

Generalized slip condition over rough surfaces

Journal:	<i>Journal of Fluid Mechanics</i>
Manuscript ID	JFM-17-S-1733
mss type:	Standard
Date Submitted by the Author:	22-Dec-2017
Complete List of Authors:	Zampogna, Giuseppe Antonio; IMFT Magnaudec, Jacques; Institut de mecanique des fluides de Toulouse, ; CNRS, Bottaro, Alessandro; Universita di Genova, DICCA;
Keyword:	Drag reduction < Flow Control, Boundary Layers

SCHOLARONE™
Manuscripts

Generalized slip condition over rough surfaces

Giuseppe A. Zampogna^{1†}, Jacques Magnaudet¹
and Alessandro Bottaro²

¹Institut de Mécanique des Fluides de Toulouse (IMFT), Université de Toulouse, CNRS,
INPT, UPS, Toulouse, France

²Dipartimento di Ingegneria Civile, Chimica e Ambientale, Università di Genova, Via
Montallegro 1, Genova, 16145, Italy

(Received ?; revised ?; accepted ?. - To be entered by editorial office)

A new macroscopic boundary condition to be used when a fluid flows over a rough surface is derived. It provides the velocity components \mathbf{u}_S tangent to the equivalent (smooth) surface in the form

$$\mathbf{u}_S = \epsilon(-\mathbf{K} \cdot \nabla p + \mathbf{L} : \mathbf{E}),$$

where the dimensionless parameter ϵ is a measure of the roughness amplitude, p and \mathbf{E} denote the pressure and strain rate tensor associated with the outer flow, respectively, and \mathbf{K} and \mathbf{L} are the surface permeability and slip tensors arising from the microscopic geometry characterizing the rough surface, respectively. This boundary condition may be considered as a natural generalization of the classical Navier slip condition. The multi-scale technique used to derive it yields a closed system of equations that allows the microscopic permeability and slip tensors to be univocally calculated, once the roughness geometry is specified. This generalized slip condition is validated by considering the flow about a rough sphere, the surface of which is covered with a hexagonal lattice of cylindrical protrusions. Comparisons with direct numerical simulations performed in the moderate-to-large Reynolds number regime allow the assessment of validity and limitations of this condition and of the mathematical model underlying the determination of the tensors \mathbf{K} and \mathbf{L} . Extensions toward superhydrophobic or partly hydrophobic surfaces are discussed by considering the macroscopic condition resulting from a combination of shear-free and no-slip microscopic behaviours.

Key words:

1. Introduction

When examined at a nano- or microscopic scale, material surfaces cannot be considered perfectly smooth. Asperities and irregularities at the various scales actually conceal the specific properties of the surface itself. The detailed study of non-smooth surfaces is a subject of growing importance that has given rise to several recent reviews, e.g. Rothstein (2010); Bhushan & Jung (2011). An important branch of this topic emerged over the last two decades as a consequence of the background accumulated on hydro- and aerodynamical drag reduction via the use of the so-called riblets (Walsh 1983; Bechert & Bartenwerfer 1989; Luchini *et al.* 1991). Because of the large separation of scales between the size of the riblets and that of the global flow phenomena that take place

† Email address for correspondence: gzampogn@imft.fr

above them, direct numerical simulations (DNS) can be prohibitively expensive in such configurations. Consequently, the Navier slip condition (Navier 1823) has been widely used to simulate fluid flows over micro-structured walls. Actually, this boundary condition was not initially designed to deal with rough surfaces. Indeed, in his 1823 seminal paper, Navier proposed a slip condition to close the flow governing equations on the sole basis of experimental considerations about the interaction between fluid particles and a generic solid wall. This condition involves a constant, λ , today called the slip length, that depends on the physical properties of the fluid and the wall. No further considerations about λ were made by Navier, for whom it was clear that only physical measurements could unveil additional information. In the last two decades, the Navier slip condition has been widely used in applications connected with superhydrophobic surfaces (Ybert *et al.* 2007; Cottin-Bizonne *et al.* 2012). Surface roughness is known to be one of the main ingredients of superhydrophobicity through the gas plastron that remains trapped within the rough layer, producing a decrease of the frictional stress acting on the fluid (Onda *et al.* 1996). Without the micro-roughnesses, the gas could not stick to the surface and the hydrophobic effect would be much reduced. Much effort has been devoted to the theoretical characterization of λ , both with and without a gas plastron (Luchini *et al.* 1991; Lauga & Stone 2003; Lauga *et al.* 2005; Davis & Lauga 2010).

Besides these classical applications related to external flows over walls, there is a rapidly growing interest for fluid flows at the nanoscale, driven by the technological evolutions that make now the fabrication of nano-channels possible. Some applications of carbon nanotubes, which exhibit exceptional and tunable hydrodynamical (Majumder *et al.* 2005), optical and electrical properties (De Nicola *et al.* 2015) are found in water desalination (Goh *et al.* 2009) and drug delivery aimed at killing cancer cells (Bhirde *et al.* 2009). The downsizing of the scales involved in fluid flow phenomena stimulated the development of molecular dynamics simulations applied to this field (Martini *et al.* 2008). At the molecular scale, a nanometric slip, with a slip length typically of the order of some tens of molecules (Bocquet & Barrat 2007), can also be identified over surfaces that are macroscopically considered hydrophilic. This has been confirmed by recent molecular dynamics simulations which revealed that velocity profiles in a Poiseuille flow exhibit deviations from profiles computed with a classical continuum model based on the Navier-Stokes equations where a no-slip condition is imposed (Liakopoulos *et al.* 2017).

The above context suggests that reconsidering the Navier slip condition to develop a model capable of predicting consistently the microscopic slip for a generic micro-structured surface is in order. A recent step towards this direction was performed by Jiménez Bolaños & Vernescu (2017) who re-derived the Navier relation by using a homogenization technique in the *small roughness* case, as defined by Luchini (2013). *Small roughness* means that the rough surface has the form $\hat{x}_3 = \epsilon h(\hat{x}_1/\epsilon, \hat{x}_2/\epsilon)$ (cf. figure 1), i.e. the surface remains geometrically similar to itself when $\epsilon \rightarrow 0$. The other significant limit discussed by Luchini (2013) is the *shallow roughness* case, $\hat{x}_3 = \epsilon h(\hat{x}_1, \hat{x}_2)$, for which the surface becomes smoother and smoother as $\epsilon \rightarrow 0$. In both instances the tangential velocity components at a virtual wall can be cast in the form of a Navier slip condition with a slip length which comes either from the solution of microscopic closure problems (Jiménez Bolaños & Vernescu 2017) or from the direct boundary integral solution of the Stokes equation (Luchini 2013). In the latter case, also a *proximity coefficient* was defined and computed, to be used whenever interactions among densely spaced wall protuberances become important (for an earlier analysis see Sarkar & Prosperetti 1996). The *shallow limit* was also considered by Kamrin *et al.* (2010) by a perturbative expansion in ϵ carried out to second order; the result is an approximate *mobility tensor* which relates the slip velocity to the mean surface normal traction. A *mobility tensor* (which

in the present paper will be called *Navier slip tensor* or simply *slip tensor* and, in the study of riblets, was named the *protrusion tensor*, cf. Bechert & Bartenwerfer 1989 and Luchini *et al.* 1991) had been previously introduced by Bazant & Vinogradova (2008) and justified also on the basis of molecular arguments; the main scope of their paper was to illustrate the power of the tensor formalism in capturing complicated effects related to the presence of anisotropic textured surfaces. Effective boundary conditions for momentum and heat transfer at rough walls, where the microscopic properties of the surfaces are transferred to an effective condition by solving closure problems at a microscopic level, have also been developed in the framework of the volume averaging method (Veran *et al.* 2009; Introïni *et al.* 2011; Guo *et al.* 2016; Pasquier *et al.* 2017).

In the present work, a multiscale homogenization technique, similar to that used by Jiménez Bolaños & Vernescu (2017), is employed to link the macroscopic and microscopic viewpoints. The main difference with those authors lies in the scalings employed to normalize the equations, which eventually lead to different equations at the various asymptotic orders. The macroscale L introduced by Jiménez Bolaños & Vernescu (2017) is $L = \mu/\sqrt{\rho\Delta P}$, with ΔP a reference pressure difference, ρ the density and μ the kinematic viscosity of the fluid. The physical case treated by Jiménez Bolaños & Vernescu (2017) results in a value of L equal to $1\text{ }\mu\text{m}$, so that the microscale l characterizing the roughness has to be exceedingly small for separation of scales to apply.

As mentioned above, developing an accurate macroscopic framework remains fully relevant nowadays, given the computational costs required to simulate microscale flow phenomena and the huge separation of scales encountered in many applications. A large amount of computational resources can be saved if a proper macroscopic condition is imposed on an equivalent smooth surface to simulate the influence of roughnesses on the large-scale flow, provided that only local fluid motions of minor significance are not captured.

A difficulty in the present problem is that the phenomena under investigation are non-homogeneous in the direction normal to the surface. Because of this, the standard homogenization technique needs to be adapted through a procedure similar to that followed by Lācis & Bagheri (2017) and Lācis *et al.* (2017). The outcome of this approach is a boundary condition which generalizes the Navier slip concept and contains in itself the formulation and boundary conditions of the microscopic problems that determine the general relationship between the outer flow characteristics (more specifically the pressure gradient tangent to the surface and the various components of the strain rate) and the geometry of the rough layer.

Section 2 presents the derivation of the generalized Navier boundary condition, highlighting the main steps of the modified homogenization approach together with the underlying assumptions. Making use of this condition with a given rough surface requires the slip and surface permeability tensors involved in the solution of two companion microscopic problems to be determined. This determination is discussed in Appendix A, together with the most important properties of these microscopic tensors, for a specific roughness geometry. The generalized boundary condition, initially developed in local surface-dependent curvilinear coordinates in §2, is extended to global Cartesian coordinates in Appendix B. In section 3, we apply this generalized boundary condition to compute the flow past a rough sphere in regimes of moderate-to-large Reynolds numbers. The numerical tool and the technical aspects involved in the computations are described in Appendix C. We coat the sphere with a hexagonal lattice of cylinders, paying special attention to the coating design in order to obtain a quasi-isotropic coverage. We then compare the solutions provided by the macroscopic approach with those of the fully-resolved simulations, which allows us to highlight the influence of the various con-

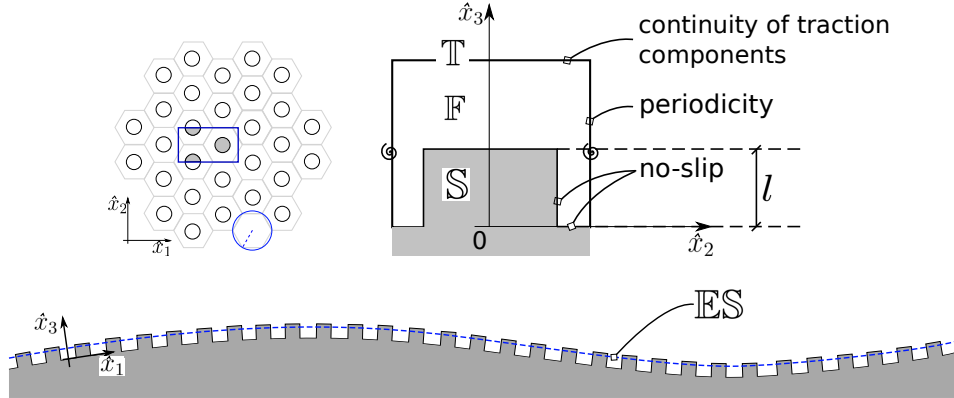


FIGURE 1. Views of the rough surface under investigation. Left: top view of a hexagonal periodic lattice on a surface. The microscopic unit cell V (blue outline) has tangential dimensions equal to \hat{l}_1 and \hat{l}_2 , respectively, both of order l . This corresponds to the so-called *small roughness limit* of Luchini (2013). The porosity ϑ is defined as $|F|/|V|$. Right: cut of the microscopic cell, at a fixed \hat{x}_1 through the center of the protrusion. The top side of the cell, denoted with T , is defined as $T = \{\hat{x}_j \in V : \hat{x}_3 = \hat{l}_3\}$. The position of T , i.e. the height of the cell \hat{l}_3 , must be of order l . Bottom: cut of the macroscopic rough surface S at a fixed \hat{x}_2 . The fictitious equivalent surface ES is represented by a dashed line (blue outline). We define the inner region (or rough layer) as the portion of space located between the surface and T , and the outer region as the portion of space standing beyond T ; ES does not necessarily separate the inner and outer regions, i.e. it does not in general coincide with T .

tributions to the boundary condition and its limitations in terms of flow regimes. We also perform a step forward towards the description of superhydrophobic surfaces, by examining the response of the flow past a sphere coated with a mixed surface, the rough layer of which involves both hydrophobic and hydrophilic parts. A summary of the main findings of the paper and suggestions for future research directions are provided in §4.

2. An effective boundary condition for rough surfaces

We consider an incompressible Newtonian fluid of constant density ρ and viscosity μ , flowing above a rough surface S as sketched in figure 1. The velocity and pressure fields in the fluid domain F are governed by the Navier-Stokes equations

$$\rho \frac{\partial \hat{u}_i}{\partial \hat{t}} + \rho \hat{u}_j \frac{\partial \hat{u}_i}{\partial \hat{x}_j} = - \frac{\partial \hat{p}}{\partial \hat{x}_i} + \mu \hat{\nabla}^2 \hat{u}_i, \quad (2.1)$$

$$\frac{\partial \hat{u}_i}{\partial \hat{x}_i} = 0, \quad (2.2)$$

with $\hat{u}_i = 0$ on the solid-fluid boundary ∂S . The roughness of the surface is provided by the presence of small protrusions distributed on a smooth surface; they are such that the surface geometry is characterized by a large separation of scales between the size L of the large-scale flow structures and the size l characterizing the protrusions. In other words, the parameter ϵ satisfies the relation

$$\epsilon = \frac{l}{L} \ll 1. \quad (2.3)$$

The particular arrangement of the protrusions (which are assumed to keep a fixed shape) forms a hexagonal lattice on the surface. Due to the large separation of scales, the effect

Generalized slip condition over rough surfaces

5

of the macroscopic curvature is negligible from a microscopic point of view and the flow can thus be assumed periodic over the cell $\mathbb{V} = \mathbb{F} \cup \mathbb{S}$.

Moreover, (2.3) allows the rough surface to be approximated by an *equivalent* smooth surface \mathbb{ES} , placed at certain distance d_ϵ from the surface on which the protrusions are stuck; d_ϵ is of $\mathcal{O}(l)$ and is unknown *a priori*. From the point of view of homogenization, \mathbb{ES} represents the homogeneous domain (i.e. a region without any distinction of phases) where macroscopic conditions can be applied. In this case, the resulting interface relation is a *slip* condition for the velocity field.

We proceed to develop the boundary condition by applying a homogenization technique to the flow in the inner region and then imposing the continuity of velocity and normal stress with the outer region at \mathbb{T} . We consider only the fluid region within the unit cell (\mathbb{F}). To normalize the equations in this region, we assume that the global pressure gradient is balanced by the local viscous term. This yields a relation that defines the order of the velocity scale U within the roughness elements as

$$\mathcal{O}\left(\frac{\Delta P}{L}\right) \sim \mathcal{O}\left(\frac{\mu U}{l^2}\right).$$

The scaled dimensionless variables are related to the dimensional ones through

$$\hat{t} = \frac{l}{U} t = \frac{\mu}{\epsilon \Delta P} t, \quad \hat{\mathbf{x}} = l \mathbf{x}, \quad \hat{p} = \Delta P p, \quad \hat{\mathbf{u}} = U \mathbf{u} = \frac{\epsilon l \Delta P}{\mu} \mathbf{u}. \quad (2.4)$$

The governing equations in \mathbb{F} thus become

$$\begin{aligned} \frac{\partial u_i}{\partial x_i} &= 0, \\ \epsilon Re \left(\frac{\partial u_i}{\partial t} + u_j \frac{\partial u_i}{\partial x_j} \right) &= -\frac{\partial p}{\partial x_i} + \epsilon \nabla^2 u_i, \end{aligned}$$

where Re is the microscale Reynolds number, defined as

$$Re = \frac{\rho U l}{\mu} = \epsilon \rho \frac{\Delta P l^2}{\mu^2}.$$

Since our goal is to develop macroscopic boundary conditions that account for the presence of the protrusions, we need to consider also the flow outside the rough layer. In this outer region, the relevant length scale is the macroscopic one, L . Denoting non-dimensional quantities in this region external to the unit cell with the superscript out we have

$$\hat{t} = \epsilon \frac{L}{U} t^{out} = \frac{l}{U} t, \quad \hat{\mathbf{x}} = L \mathbf{x}^{out}, \quad \hat{p} = \Delta P p^{out}, \quad \hat{\mathbf{u}} = \frac{U}{\epsilon} \mathbf{u}^{out} = \frac{l \Delta P}{\mu} \mathbf{u}^{out}, \quad (2.5)$$

where lengths are normalized with the macroscopic scale L . We have assumed that the velocity scale in the outer region is $1/\epsilon$ times larger than the velocity scale U within the rough layer; this is consistent with the fact that the inner-outer problem is coupled through a unique time scale, l/U . These normalizations will be used later to infer boundary conditions for the microscale problem.

For the sake of simplicity, we develop the model in the case of planar surfaces covered by a lattice of hexagonal periodic cells. The generalization to non-planar surfaces will be addressed later. In this case the pattern is periodic along the directions tangential to the plane, i.e. x_1 and x_2 . Figure 1 indicates that the flow characteristics only experience slow variations in the x_1 and x_2 directions, but may vary much faster in the direction

normal to the plane, x_3 . For this reason, within the rough layer, we can use the multiscale homogenization theory described by Mei & Vernescu (2010); we introduce the fast (microscopic) and slow (macroscopic) variables, $\mathbf{x} = (x_1, x_2, x_3)$ and $\mathbf{x}' = \epsilon(x_1, x_2)$, and the expansions

$$\mathbf{u} = \mathbf{u}^{(0)} + \epsilon \mathbf{u}^{(1)} + \dots, \quad p = p^{(0)} + \epsilon p^{(1)} + \dots \quad (2.6)$$

where $\mathbf{u}^{(i)}$ and $p^{(i)}$ are functions of $(\mathbf{x}, \mathbf{x}', t)$. Noting that

$$\frac{\partial}{\partial x_i} \rightarrow \frac{\partial}{\partial x_i} + \epsilon \frac{\partial}{\partial x'_i} \quad \text{for } i = 1, 2, \quad (2.7)$$

substituting (2.6) in the Navier Stokes equations and collecting terms at every order in ϵ , we obtain at leading order

$$\frac{\partial u_i^{(0)}}{\partial x_i} = 0 \quad \forall i, \quad (2.8)$$

$$0 = -\frac{\partial p^{(0)}}{\partial x_i} \quad \forall i, \quad (2.9)$$

and at next order

$$\frac{\partial u_j^{(0)}}{\partial x'_j} + \frac{\partial u_i^{(1)}}{\partial x_i} = 0, \quad \forall i, j = 1, 2; \quad (2.10)$$

$$0 = -\frac{\partial p^{(1)}}{\partial x_i} - \frac{\partial p^{(0)}}{\partial x'_i} + \frac{\partial^2 u_i^{(0)}}{\partial x_j \partial x_j}, \quad \forall i, j = 1, 2; \quad (2.11)$$

$$0 = -\frac{\partial p^{(1)}}{\partial x_3} + \frac{\partial^2 u_3^{(0)}}{\partial x_j \partial x_j}, \quad \forall j, \quad (2.12)$$

under the hypothesis that Re is at most $\mathcal{O}(\epsilon)$. This implies that l is at most $\mathcal{O}(\mu/\sqrt{\rho \Delta P})$ which, considering for example the physical parameters of the case treated by Jiménez Bolaños & Vernescu (2017), translates into $l \lesssim \mathcal{O}(1 \mu m)$. Furthermore, the outer Reynolds number, based on U^{out} and L , is large and can be up to ϵ^{-1} .

From (2.9) one deduces that $p^{(0)} = p^{(0)}(\mathbf{x}', t)$, i.e. the pressure at leading order varies only over the macroscale. To solve the flow at leading order, we consider the problem governed by (2.8), (2.11) and (2.12). The corresponding unknowns are $u_i^{(0)}$ and $p^{(1)}$ forced by the macroscopic pressure field $p^{(0)}$. In order to formally write the solution, we also need to consider the conditions imposed at the boundaries of \mathbb{F} . As indicated in figure 1, periodicity holds along directions x_1 and x_2 tangential to the surface, whereas the no-slip condition

$$u_i^{(0)} = 0 \quad (2.13)$$

holds at the common boundary, $\partial\mathbb{S}$, between \mathbb{F} and \mathbb{S} . At the top surface \mathbb{T} of the microscopic cell ($x_3 = l_3 = \hat{l}_3/l$), the continuity of tractions implies

$$\hat{T}_{jk}(\hat{\mathbf{u}}^{(0)})n_k = \hat{T}_{jk}(\hat{\mathbf{u}}^{out})n_k, \quad (2.14)$$

where \hat{T}_{jk} is the dimensional stress tensor and n_k denotes the normal vector which, in the present case, corresponds to \mathbf{e}_3 . In outer scales the fictitious surface $\mathbb{E}\mathbb{S}$ corresponds to $x_3^{out} = 0$. Using normalizations (2.4) and (2.5), (2.14) yields

$$\left(\frac{\partial u_i^{(0)}}{\partial x_3} + \frac{\partial u_3^{(0)}}{\partial x_i} \right) = \left(\frac{\partial u_i^{out}}{\partial x_3^{out}} + \frac{\partial u_3^{out}}{\partial x_i^{out}} \right) \quad i = 1, 2 \quad (2.15)$$

and

$$-p^{(0)} + 2\epsilon \frac{\partial u_3^{(0)}}{\partial x_3} = -p^{out} + 2\epsilon \frac{\partial u_3^{out}}{\partial x_3^{out}}, \quad (2.16)$$

which, at leading order, reduces to

$$p^{(0)} = p^{out}. \quad (2.17)$$

While (2.15) must be used when seeking an appropriate form of $u_i^{(0)}$, (2.17) is a condition for the pressure at leading order, $p^{(0)}$, that appears as a source term in (2.11) for $u_i^{(0)}$. Continuity of velocity components on \mathbb{T} imposes $\hat{u}_i^{(0)} = \hat{u}_i^{out}$, which, in dimensionless form, reads $\epsilon u_i^{(0)} = u_i^{out}$. This does not yield any further information on the solution at leading order. The solution of (2.8), (2.11) and (2.12) may be written in the form

$$u_i^{(0)} = -K_{ij} \frac{\partial p^{(0)}}{\partial x_j'} + L_{il3} \left(\frac{\partial u_l^{out}}{\partial x_3^{out}} + \frac{\partial u_3^{out}}{\partial x_l^{out}} \right) |_{x_3=l_3}, \quad j, l = 1, 2, \forall i, \quad (2.18)$$

$$p^{(1)} - p_0^{(1)}(\mathbf{x}') = -A_j \frac{\partial p^{(0)}}{\partial x_j'} + B_{l3} \left(\frac{\partial u_l^{out}}{\partial x_3^{out}} + \frac{\partial u_3^{out}}{\partial x_l^{out}} \right) |_{x_3=l_3} \quad j, l = 1, 2, \quad (2.19)$$

where K_{ij} and L_{il3} (resp. B_{l3} and A_j) are unknown tensors (resp. vectors). Given the previous assumptions and boundary conditions, only part of their coefficients can be different from zero, namely

- $K_{11}, K_{21}, K_{31}, K_{12}, K_{22}, K_{32};$
- $L_{113}, L_{213}, L_{313}, L_{123}, L_{223}, L_{323};$
- $B_{13}, B_{23};$
- $A_1, A_2.$

Substituting (2.18) into (2.8), (2.11) and (2.12), it is readily found that the coefficients satisfy the following problems

$$\begin{cases} \frac{\partial A_j}{\partial x_i} - \nabla^2 K_{ij} = \delta_{ij}, & j = 1, 2, \forall i \\ \frac{\partial K_{ij}}{\partial x_i} = 0 & j = 1, 2, \forall i, \\ K_{ij} = 0 \text{ on } \partial \mathbb{S}, \\ \frac{\partial K_{jl}}{\partial x_3} + \frac{\partial K_{3l}}{\partial x_j} = 0, \text{ on } \mathbb{T} & l = 1, 2, \forall j, \\ K_{ij} \text{ periodic along the } x_1 \text{ and } x_2 \text{ directions.} \end{cases} \quad (2.20)$$

Similarly, substituting (2.19) into (2.11) and (2.12) yields

$$\begin{cases} -\frac{\partial B_{l3}}{\partial x_i} + \nabla^2 L_{il3} = 0, & l = 1, 2, \forall i \\ \frac{\partial L_{il3}}{\partial x_i} = 0 & l = 1, 2, \forall i, \\ L_{il3} = 0 \text{ on } \partial \mathbb{S}, \\ \frac{\partial L_{pl3}}{\partial x_3} + \frac{\partial L_{3l3}}{\partial x_p} = \delta_{lp}, \text{ on } \mathbb{T} & l = 1, 2, \forall j, \\ L_{il3} \text{ periodic along the } x_1 \text{ and } x_2 \text{ directions.} \end{cases} \quad (2.21)$$

To ensure uniqueness of the solution to (2.20) and (2.21), we also impose

$$\langle A_j \rangle = 0 \text{ and } \langle B_{j3} \rangle = 0 \quad (2.22)$$

for $j = 1, 2$, where the volume average over a unit cell $\langle \cdot \rangle$ is defined as

$$\mathcal{G} = \langle G \rangle := \frac{1}{|\mathbb{V}|} \int_{\mathbb{F}} G dV, \quad (2.23)$$

with the integral evaluated only over \mathbb{F} since G is only defined in the fluid phase. Taking the volume average of (2.18), noting that \mathbf{u}^{out} , $p^{(0)}$ and $p_0^{(1)}$ do not depend on the fast variable \mathbf{x} and making use of the condition (2.22), we obtain

$$\langle u_i^{(0)} \rangle = -\mathcal{K}_{ij} \frac{\partial p^{(0)}}{\partial x'_j} + \mathcal{L}_{il3} \left(\frac{\partial u_l^{out}}{\partial x_3^{out}} + \frac{\partial u_3^{out}}{\partial x_l^{out}} \right) |_{x_3^{out}=0}, \quad j, l = 1, 2, \forall i, \quad (2.24)$$

with $\mathcal{K}_{ij} = \langle K_{ij} \rangle$, and $\mathcal{L}_{ij3} = \langle L_{ij3} \rangle$.

Furthermore we have

$$\langle p^{(1)} \rangle = \vartheta p_0^{(1)}, \quad \text{with } \vartheta = \frac{|\mathbb{F}|}{|\mathbb{V}|}.$$

It is important to notice that, after averaging (2.18), the microscopic domain has shrunk to a single point along the normal-to-the-surface direction, i.e. $x_3 = l_3$ in (2.18) and (2.19) has become $x_3^{out} = 0$. In fact, (2.24) is a homogeneous equation that does not depend on \mathbf{x} any more and applies only at the surface \mathbb{ES} . To better appreciate (2.24) which is actually an equivalent boundary condition for the *outer* flow to be imposed on a fictitious wall, it is convenient to rewrite it with the help of a pressure normalized with a dynamic scale, i.e. $\rho(U^{out})^2$ (velocity and position maintain their scales, i.e. $U^{out} = U/\epsilon$ and L , cf. (2.5)). In dimensionless form, the fictitious wall boundary condition becomes

$$u_i = -\epsilon^2 Re^{out} \mathcal{K}_{ij} \frac{\partial p}{\partial x_j} + \epsilon \mathcal{L}_{il3} \left(\frac{\partial u_l}{\partial x_3} + \frac{\partial u_3}{\partial x_l} \right) |_{\mathbb{ES}}, \quad (2.25)$$

where the outer Reynolds number is defined as $Re^{out} = \rho U^{out} L / \mu$. Equation (2.25) is valid for planar surfaces parallel to the plane $x_3 = 0$. For the planar surface considered up to now, \mathcal{K}_{3j} and \mathcal{L}_{3l3} are zero, owing to the antisymmetry of the microscopic non-diagonal components K_{3j} and L_{3l3} (see Appendix A). Hence, according to (2.25), the wall normal velocity u_3 is zero on \mathbb{ES} . For a generic surface, (2.25) may be generalized as

$$u_i = -\epsilon^2 Re^{out} \mathcal{K}_{ij} \frac{\partial p}{\partial x_j} + \epsilon \mathcal{L}_{ilk} \left(\frac{\partial u_l}{\partial x_k} + \frac{\partial u_k}{\partial x_l} \right) |_{\mathbb{ES}}. \quad (2.26)$$

In (2.26), the tensors \mathcal{K}_{ij} and \mathcal{L}_{ilk} are obtained by applying to their counterpart in (2.25) the mapping from the Cartesian coordinates to the local system of reference of the surface. In other words, we are assuming that the unit cell is cubic also in the case of curved surfaces. This is a good approximation if the separation of scales is sufficiently large, i.e. the curvature at the microscale is negligible with respect to its counterpart at the macroscale. With the notation used in (2.26), it is not obvious that the wall normal velocity is zero; the proof of this is given in Appendix B.

Equation (2.26) expresses the average velocity in the cell as the sum of two parts. The first term on the right-hand side resembles Darcy's law, where \mathcal{K}_{ij} plays the role of a permeability. We term it the *surface permeability*, since it expresses the ability of the fluid to permeate the rough layer under the effect of a tangential pressure gradient. The second term on the right-hand side represents the tensorial form of the Navier

slip condition (Navier 1823), with the classical slip length changed into the slip tensor \mathcal{L}_{ijk} . This condition can be viewed as a generalization of the celebrated Beavers-Joseph condition at a permeable wall (Beavers & Joseph 1967). It is worth noting that condition (2.26) was developed under the assumption that Re^{out} is up to $\mathcal{O}(\epsilon^{-1})$. This implies that, whenever Re^{out} is small compared to unity, the Darcy contribution is negligible compared to the Navier term. Conversely, if Re^{out} is of $\mathcal{O}(\epsilon^{-1})$, the two terms in (2.26) are formally of comparable magnitude. Their relative importance will be assessed later. Finally it must be observed that, as a consequence of the restriction on Re^{out} , when the surface is smooth, the no-slip condition is recovered by considering the limit $\epsilon \rightarrow 0$. Thus, (2.26), represents a general boundary condition that applies to any *small roughness* surface, the amplitude of which is measured by ϵ .

3. Application to a rough sphere in a uniform stream

Condition (2.26) holds over arbitrary surfaces, provided that the effective tensors are computed for the associated microscopic geometry. The computation and properties of the microscopic solutions are discussed in Appendix A. Here we apply this condition, through the resulting distributions of the permeability and slip tensor components at the equivalent fluid-solid surface, to study the dynamics of the flow past a rough spherical particle (RSP). The overall objective of this section is to discuss and compare the results obtained through a pointwise description with those provided by the macroscopic approach in order to assess the applicability and accuracy of the homogenization framework.

3.1. Designing a rough sphere

The RSP is built by covering a sphere with a hexagonal lattice of cylinders (cf. figure 1). Unfortunately, neither this lattice, nor any other planar lattice, obtained through the periodic repetition of a single planar figure can cover a sphere. For this reason, we seek a distribution of protrusions as isotropic as possible and as close as possible to that introduced in figure 1, so that the global dynamics of the RSP may be compared with that of a smooth spherical particle (SSP). A quasi-isotropic distribution is achieved by discretizing the sphere as a quasi-regular icosahedron. The latter is a polyhedron characterized by twelve special points, the poles, that divide the sphere into fifteen portions (ten of them triangular and the other five rectangular), and by a frequency ξ giving the number of sides between two consecutive poles belonging to a triangular portion (see figure 2, top). The residual non-homogeneity of the distribution at the surface of the icosahedron arises from the presence of the twelve poles (figure 2, bottom). Despite this imperfect distribution, it will be shown later that the homogenization approach may be applied successfully. Different examples of coatings are shown in figure 2 (central row), for different ξ and ϑ . These two parameters univocally define the dimensions of the protrusions, the shape of which is characterized by a radius r and a height h . The latter is a free parameter of the design, which in the present case is set to l , the side length of each face of the icosahedron. The macroscopic scale L is set to R^{inn} , the radius of the smooth sphere at the surface of which the protrusions are placed. Figure 3 shows how the parameter $\epsilon = l/L = h/R^{inn}$ and the total number of protrusions, N , depend on ξ . A small decrease in ϵ is seen to correspond to a large increase in ξ , hence in the number of protrusions. This means that performing a direct numerical simulation of the RSP with a small ϵ (i.e. in the limit of a homogeneous roughness) would imply a high computational complexity. Clearly, the macroscopic analogy becomes very useful in this limit. In this analogy, two related but distinct objects play a role. The first of them is

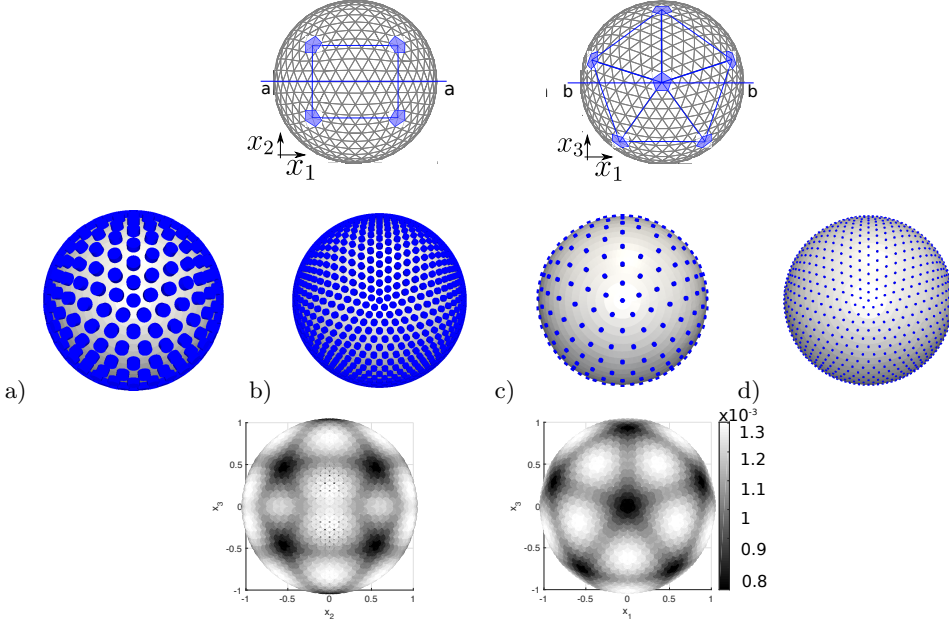


FIGURE 2. Top row: icosahedral discretization of a sphere ($\xi = 8$), front (left) and top (right) view. A protrusion is placed at each vertex of the icosahedron. Central row: examples of macroscopic spheres covered by cylindrical protrusions for the following values of the parameters: $\vartheta = 0.60$ (a,b), $\vartheta = 0.95$ (c, d), with $\xi = 6$ (a, c) and $\xi = 12$ (b, d). Bottom row: distribution of the non-homogeneity in the coverage of the icosahedron surface for $\xi = 12$ (front and top views, respectively). The gray scale indicates the area of each face of the icosahedron; this area decreases as the poles are approached.

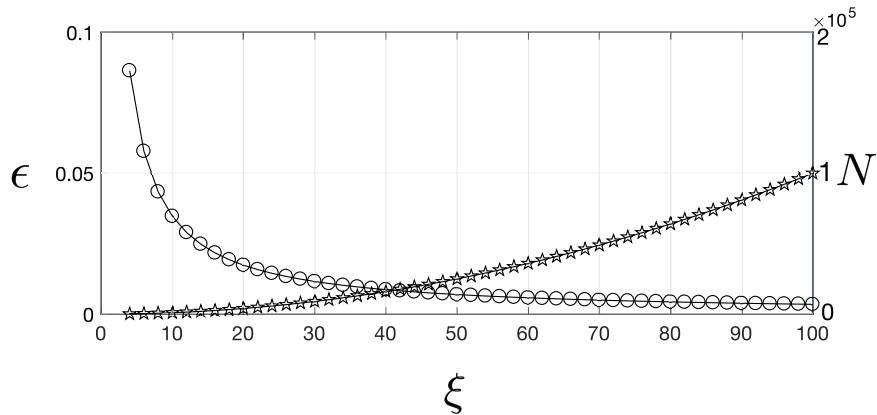


FIGURE 3. Variation of ϵ (circles, scale on the left vertical axis) and the number of protrusions N (stars, scale on the right vertical axis) with respect to the frequency ξ of the icosahedron.

the RSP, characterized by R^{inn} and $R^{out} = R^{inn}(1 + \epsilon)$, the radius of the *outer spherical particle* defined as the smooth sphere encompassing the whole RSP. The second is the *equivalent spherical particle* (ESP), the radius of which is R^{eq} (see figure 4). The ESP has the same macroscopic physical properties as the corresponding RSP and is expected to behave in the same manner, provided that the condition (2.26) is imposed over its surface. The equivalent radius depends in principle on the shape of the protrusions and

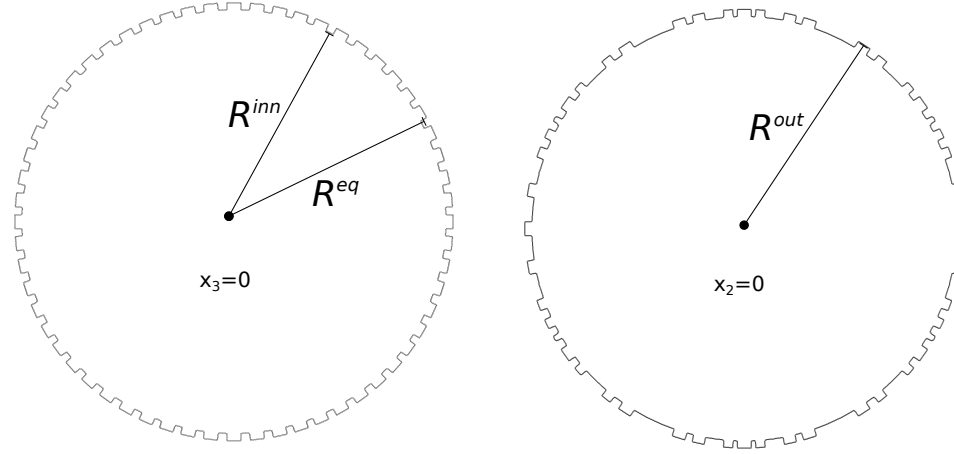


FIGURE 4. Cut of the simulated RSP across two orthogonal planes. The non-homogeneity in the distribution of the protrusions can be observed. The inner radius, R^{inn} , the equivalent radius, R^{eq} , and the outer radius, R^{out} , are indicated.

on the parameters ϑ and ξ . One expects R^{eq} to lie in between R^{inn} and R^{out} ; this will be confirmed later in a selected case.

3.2. The reference DNS

We are now in a position to perform direct numerical simulations of a uniform flow past the RSP we just designed. The standard computational domain is a parallelepiped of size $200 \times 80 \times 80$, in R^{inn} -units. A zero velocity gradient boundary condition is imposed at the outlet (Versteeg & Malalasekera 2007). As detailed in Appendix C, thanks to this domain size and outlet condition, the physical quantities relevant to the sphere-induced disturbance are not influenced by the outer boundaries in the considered range of Reynolds number. A constant inlet velocity $(1, 0, 0)$ is imposed at $x_1 = 0$, while symmetry conditions are imposed on the x_2 and x_3 surfaces to simulate an unbounded domain.

Before comparing macroscopic simulations and DNS results, we analyze the latter in the case of a rough sphere with $Re^{out} = 100$ based on the sphere inner diameter), $\vartheta = 0.6$ and $\xi = 12$, for which $\epsilon = 0.029$ (a zoom of the grid used to discretize the flow close to the particle surface is provided in figure 21). Figure 5 shows the geometry of the corresponding spherical particle, with the iso-surface corresponding to $u_1 = 0$ (left frame). In the right frame, the iso-contours of u_1 are represented, together with the separation angle, α_S , and the recirculation length, l_r . The latter can be measured with respect to the inner or outer particle radius, yielding values l_r^{inn} and l_r^{out} , respectively. Figure 6 displays some iso-contours of velocity components u_1 and u_3 in the cross-sectional plane $x_2 = 0$, in the case of a SSP with $R = 1$ (red) and $R = R^{out}/R^{inn}$ (green), and the RSP (black). Differences between the three fields are of order ϵ , as predicted by Amirat *et al.* (2001). While the fields computed for the case of the RSP and the SSP with $R = R^{out}/R^{inn}$ are very similar in the region close to the sphere, more significant changes arising from the presence of the rough layer can be observed in the wake.

Table 1 reports the values of several quantities characterizing the flow past the particle, especially the normalized drag force, F_D , split into its viscous, F_V , and pressure, F_P , components. As the comparison with the SSP reveals, introducing a rough surface signi-

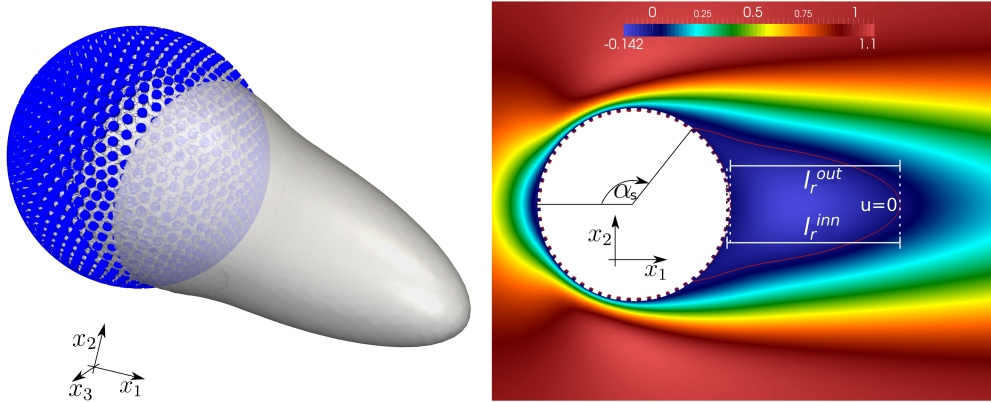


FIGURE 5. Flow past a RSP; the iso-surface corresponding to $u_1 = 0$ is shown in grey on the left. On the right, iso-contours of u_1 are represented with colours. The thin red line corresponds to the iso-contour $u_1 = 0$. The recirculation length may be defined with respect to either the inner radius (l_r^{inn}) or the outer radius (l_r^{out}). The separation angle α_S is measured clockwise.

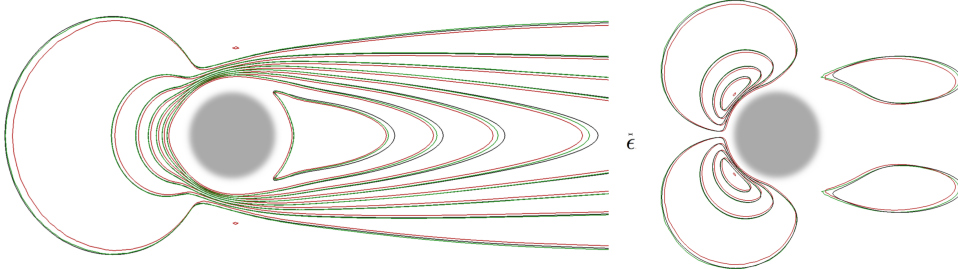


FIGURE 6. Isocontours of u_1 (left) and u_3 (right) at $x_2 = 0$ ($x_2 = 0$ in this plane). Values of the u_1 (resp. u_3) velocity component in the left (right) frame are equally spaced from -0.132 to $+1.105$ (respectively, from -0.475 to 0.475). The red and green lines corresponds to a SSP with a no-slip condition at $R = 1$ and $R = R^{out}/R^{inn}$, respectively, and the black lines to a RSP with $\vartheta = 0.6$ and $\xi = 12$. The size of ϵ is shown to scale at the center of the figure.

fificantly increases the pressure drag and decreases its viscous counterpart. The changes in the total drag force are however quite small. Note that, due to the weakly anisotropic distribution of the protrusions, the x_2 - and x_3 -components of the force acting on the RSP (not shown) are not strictly zero. However the corresponding values are very small and rapidly tend to zero as ξ increases. According to the values of α_S and l_r^{out} reported in the table, the rough surface is found to slightly delay separation and increase the recirculation length.

3.3. Simulation using the macroscopic boundary condition

Up to now, the flow dynamics past the RSP was analyzed using a *pointwise* approach. To make the comparison between previous DNS results and those obtained with the ESP, we make use of the macroscopic analogy briefly discussed at the end of the previous section. To establish a one-to-one link between the macroscopic fields and those resolved at each scale in the DNS, it is sufficient to divide the *rough layer* into microscopic cells such as that shown in grey in the central frame of figure 7 and, for each field, calculate the average defined in (2.23). Each microscopic elementary cell corresponds to a macroscopic point on the ESP surface, identified by the center of the cell's face belonging to the sphere. Once the averaged fields have been extracted from the DNS, comparisons can

	F_P	F_V	F_D	$\alpha_S(\circ)$	l_r^{inn}	l_r^{out}
RSP, $\vartheta = 0.6$, $\xi = 12$	0.261	0.186	0.447	128.3	1.840	1.810
SSP, $R = 1$	0.201	0.228	0.429	128.1	1.802	--
SSP, $R = R^{out}/R^{inn}$	0.202	0.232	0.434	127.3	--	1.756

TABLE 1. Several characteristics of the flow past a SSP and a RSP at $Re^{out} = 100$ (the fluid density, upstream velocity and sphere inner radius are set equal to unity). The drag force, F_D , is split into viscous, F_V , and pressure, F_P , components. The separation angle and recirculation length are defined in figure 5.

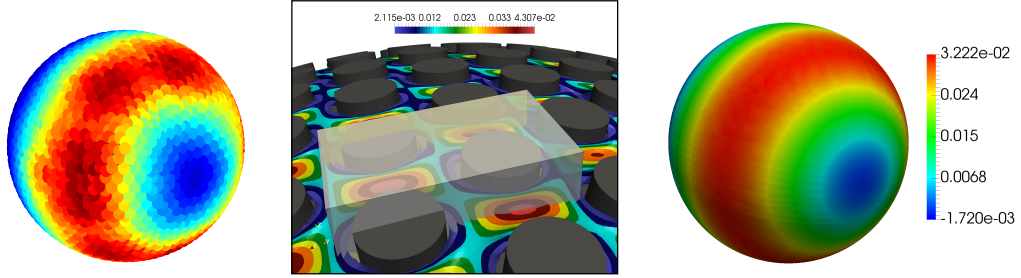


FIGURE 7. Comparison of the velocity component u_1 on the sphere, computed with the macroscopic model (2.26) on the right, and extracted from the reference DNS (left). To pass from one approach to the other, we apply the volume average operator (2.23) over the microscopic cell V sketched in grey in the central frame. The surface of the RSP is divided into elementary cells to deduce *a posteriori* the averaged fields from the DNS (the microscopic distribution is seen in the central frame in the form of u_1 -iso-contours on a surface slightly above $R = 1$). The average over each cell may then be compared with the value provided by the macroscopic approach at the corresponding point of the ESP boundary.

be performed within two different orthogonal half-planes intersecting the sphere (eg. those denoted as aa and bb in figure 2). Condition (2.26) is imposed at either $R = 1$ or $R = R^{out}/R^{inn}$ and we found the results to be indistinguishable to graphical accuracy. In the situation to be described below, values of the surface permeability and slip tensor are $\mathcal{K}_{11} = 0.01096$, $\mathcal{K}_{22} = 0.01103$, $\mathcal{L}_{113} = 0.00975$ and $\mathcal{L}_{223} = 0.009821$. These values were computed as described in Appendix A, using a microscopic cell with $l_3 = \sqrt{3}l$.

A first qualitative comparison of the prediction provided by the two approaches for the main (streamwise) component of the velocity over the spherical particle may be inferred from the left and right frames of figure 7. The small differences observed between the two distributions are due to the non-homogeneity of the lattice covering the RSP. The influence of the weak differences, $\mathcal{K}_{11} - \mathcal{K}_{22}$ and $\mathcal{L}_{113} - \mathcal{L}_{223}$, resulting from this non-homogeneity may be quantified by examining the surface velocity distributions in figure 8. Variations not exceeding 3–4% are observed between the maxima of a given component, depending on whether it is measured within the aa or bb cross-sectional plane.

Figure 9 shows the distributions of the surface vorticity and pressure in the cross-sectional planes corresponding to lines aa and bb in figure 2. A good agreement between

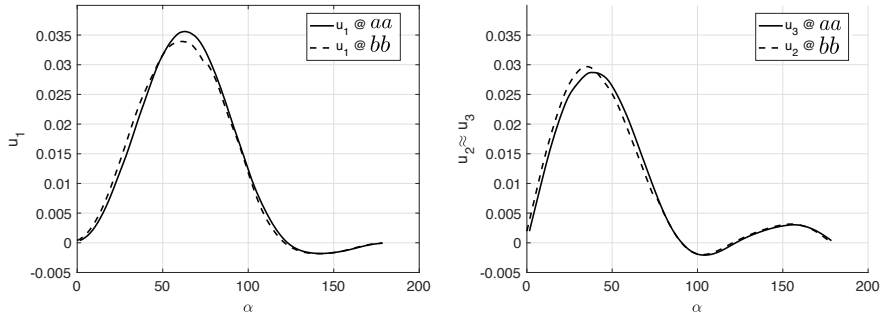


FIGURE 8. Influence of the lattice inhomogeneities on the surface velocity distributions determined using (2.26) along the aa and bb cross-sectional planes.

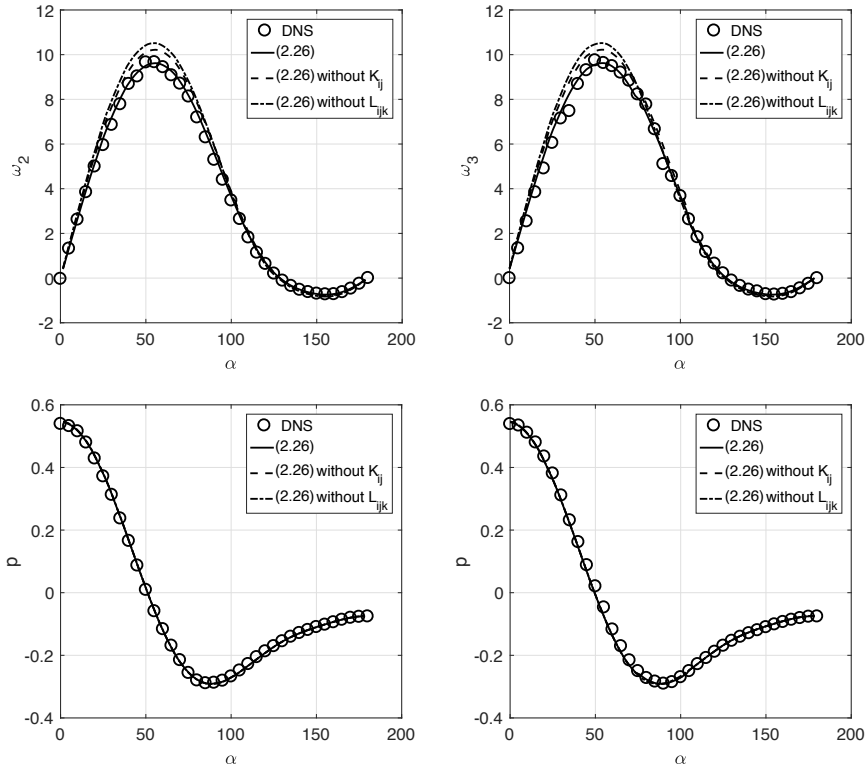


FIGURE 9. Surface distribution of the non-zero components of the surface vorticity ω_j and pressure p along aa (left) and bb (right). The circles represent the results extracted from the DNS while the lines indicate three different simulations using (2.26) on the ESP, with and without the contribution of the surface permeability or slip.

the prediction based on condition (2.26) (solid line) and the values extracted from the DNS (circles) is observed. The small oscillations in the DNS profiles of ω_i are due to the defects in the periodicity and homogeneity of the lattice that coats the sphere. Differences in the pressure field cannot be seen at that scale. The solutions computed without the contribution of the surface permeability (dashed lines) exhibit non negligible differences in the vorticity distribution around the sphere's equator. As discussed in section 2, the

	F_P	F_V	F_D	α_S	l_r
RSP, $\vartheta = 0.6$, $\xi = 12$	0.198	0.228	0.426	128.3	1.825*
ESP, $R^{eq} = 1$	0.200	0.226	0.426	128.5	1.698
ESP, $R^{eq} = 1$, with $\mathcal{K}_{ij} = 0$	0.200	0.232	0.432	128.4	1.690
ESP, $R^{eq} = 1$, with $\mathcal{L}_{ijk} = 0$	0.201	0.269	0.470	127.5	1.714
ESP, $R^{eq} = R^{out}/R^{inn}$	0.198	0.221	0.419	128.5	1.740

TABLE 2. Global quantities characterizing the flow past the spherical particle, evaluated with a macroscopic approach (the value of l_r with the asterisk is computed by considering the average between l_r^{inn} and l_r^{out} ; in the macroscopic framework, deviations of $\mathcal{O}(\epsilon)$ from this value are allowed).

contribution of the surface permeability is important in this Reynolds number range, since Re^{out} is of $\mathcal{O}(\epsilon^{-1})$. This feature does not necessarily prove that (2.26) approximates the solution better than the classical Navier slip condition. It simply means that taking into account the influence of the pressure gradient term is required if the *effective* slip tensor is computed in the way discussed in Appendix A. As the dash-dotted lines in figure 9 show, the solution degrades further if the slip contribution involved in (2.26) is not taken into account.

Table 2 summarizes some flow characteristics obtained using the aforementioned options. The values in the first row of tables 1 and 2 refer to the same simulation. Nevertheless, the two series of values for the force are different because they were computed using the pointwise approach in the former case, while the averaged fields were used in the latter one (see Appendix C). The results of four distinct simulations carried out past the ESP are displayed, which allows the influence of the exact definition of the sphere radius ($R = 1$ or $R = R^{out}/R^{inn}$) where (2.26) is imposed and that of the surface permeability and slip to be disentangled.

From a global point of view, the model is seen to approximate the DNS results well, as differences between the models are smaller than order ϵ . In particular, looking at the predictions on the ESP with and without \mathcal{K}_{ij} , we note a slight worsening in the evaluation of F_V in the latter case, while F_P remains unaltered, in agreement with the profiles reported in figure 9. The simulations carried out without \mathcal{L}_{ijk} overestimate significantly the vorticity near the particle's equator, hence the viscous component of the drag force. Indeed, neglecting the contribution of the slip tensor deeply underestimates the tangential velocity at the particle surface, reducing its maximum to approximately one fourth that obtained using (2.26) which yields an overestimate of the velocity gradient in the radial direction.

According to table 2, the differences obtained by imposing the ESP radius either to $R = 1$ or to $R = R^{out}/R^{inn}$ are very small and nothing can be concluded regarding the exact position of the equivalent surface. This is in agreement with the level of accuracy of the theory: since we are computing an $\mathcal{O}(\epsilon)$ approximation of the flow, we can only conclude that the relative difference between the radius of the ESP and that of the SSP is also of $\mathcal{O}(\epsilon)$. Determining the position of the interface with more accuracy would require a higher-order approximation of the solution, which can only be obtained by carrying out the homogenization procedure up to $\mathcal{O}(\epsilon^2)$.

Another point has to be mentioned regarding the choice of l_3 . The only indication provided by the homogenization theory about this choice is that l_3 has to be of $\mathcal{O}(\epsilon)$.

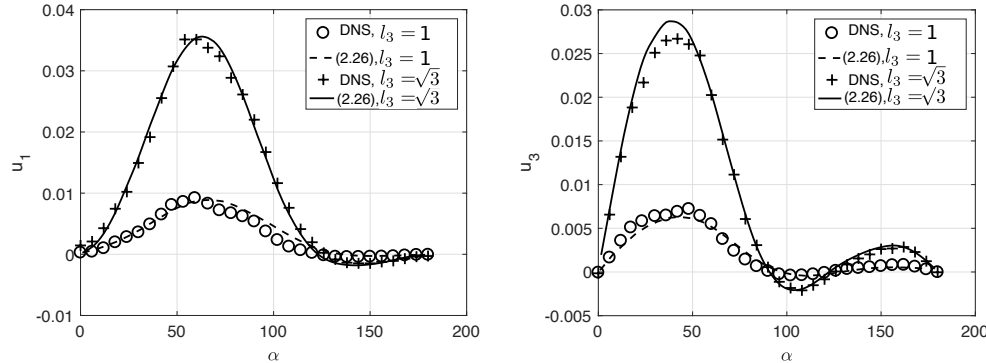


FIGURE 10. Nonzero components of the surface velocity sampled within the aa cross-sectional plane. The solid (resp. dashed) line represents the macroscopic solution with \mathcal{K}_{ij} and \mathcal{L}_{ijk} computed over a cell with $l_3 = \sqrt{3}$ (resp. $l_3 = 1$). Profiles with symbols are extracted from a single DNS, by changing the thickness over which the results are averaged.

In particular, each l_3 yields a different value for the permeabilities \mathcal{K}_{ij} , hence a different value of the velocity at the surface over which (2.26) is applied. This is fully consistent with the macroscopic framework within which the results have to be interpreted. Figure 10 displays the non-zero surface velocity components sampled within the cross-sectional plane aa . The cell-averaged velocity resulting from the DNS was extracted using two different elementary cells corresponding to those used to compute the effective tensors, such that l_3/l is either equal to 1 or to $\sqrt{3}$. Both distributions are found to agree well with those predicted on the macroscopic approach based on the corresponding \mathcal{K}_{ij} and \mathcal{L}_{ijk} . That the averaged surface velocity changes with the thickness of the cell along the direction normal to the surface is directly linked to the fact that the phenomenon under consideration is not homogeneous along that direction.

3.4. Beyond the restriction $Re^{out} \leq \epsilon^{-1}$

The condition (2.26) was developed under the assumption that the macroscopic Reynolds number is not higher than $\mathcal{O}(\epsilon^{-1})$. Many natural phenomena or engineering applications involving flows over rough surfaces take place in regimes such that Re^{out} is much higher than this theoretical restriction. To check the validity of the model for $Re^{out} = \mathcal{O}(\epsilon^{-2})$, we performed a DNS of the flow past the RSP (still with $\vartheta = 0.6$ and $\xi = 12$) at $Re^{out} = 10^3$. At this Reynolds number, the flow is fully unsteady and turbulence is developing in the wake. Figure 11 displays the evolution of the drag force acting on the RSP over a sample time interval, together with the prediction of the macroscopic approach based on (2.26), with or without the contribution of the surface permeability. The DNS prediction of Orr *et al.* (2015) obtained on a smooth sphere is also shown as a reference. DNS and macroscopic distributions of the time-averaged surface vorticity and pressure in the cross-sectional planes aa and bb as compared in figure 12. While differences found among the pressure distributions remain small, those observed in the equatorial region on the surface vorticity are significant. Clearly (2.26) underpredicts the surface vorticity in that region, hence the viscous drag force. The poor prediction of the macroscopic approach in this case may be readily understood by noting that the microscale Reynolds number, $Re = \rho Ul/\mu$, characterizing the flow within each cavity embedded in the rough layer is equal to 0.84, much larger than $\epsilon = 0.029$. Hence values of the microscopic tensor components K_{ij} and L_{ijk} computed on the basis of a local flow within the rough layer governed by Stokes equations are no longer valid. This limitation

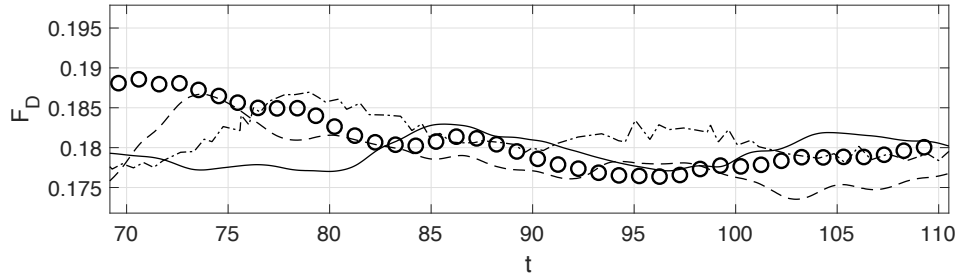


FIGURE 11. Evolution of the drag force acting on the sphere for different simulations at $Re^{out} = 10^3$. Circles: DNS of the RSP, solid (resp. dashed) line: simulations with (2.26) on the ESP, with (resp. without) the contribution of the surface permeability, dash-dotted line: DNS result of Orr *et al.* (2015) on a smooth sphere.

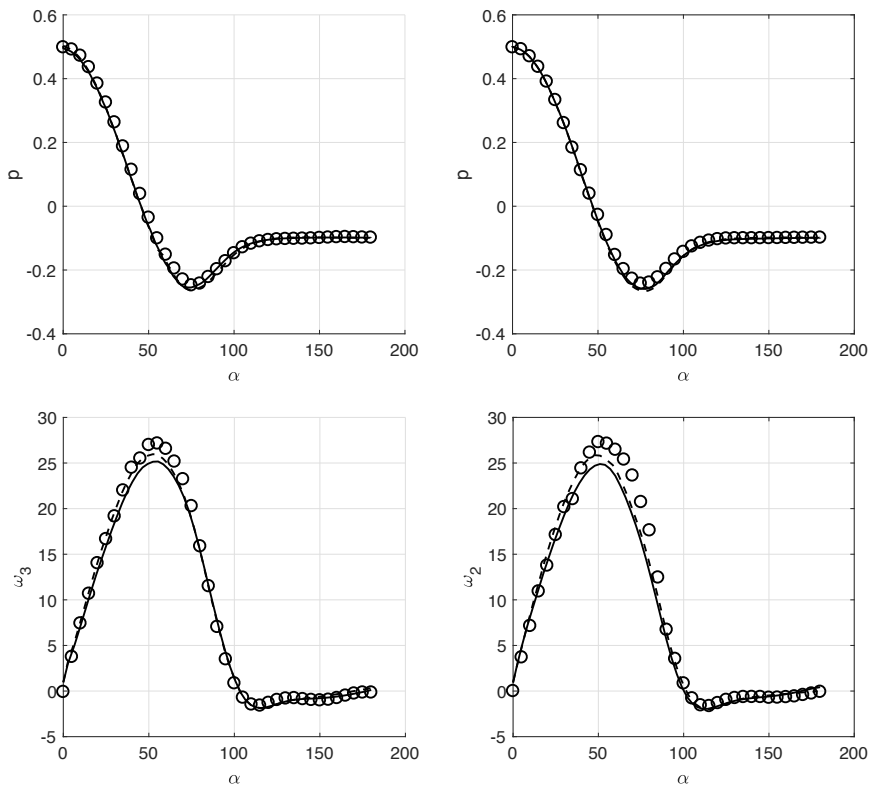


FIGURE 12. Surface pressure and nonzero components of the surface vorticity within the *aa* (left) and *bb* (right) cross-sectional planes for $Re^{out} = 10^3$. Circles: DNS, solid (resp. dashed) line: macroscopic results based on (2.26) with (resp. without) the contribution of the surface permeability.

was already considered by Zampogna & Bottaro (2016) who modified the microscopic problems by incorporating Oseen's correction to compute the permeability tensor in the case of inertia-dominated flows through rigid porous media. The potential of this approach to fix the above issue in the present problem will be examined in a future work.

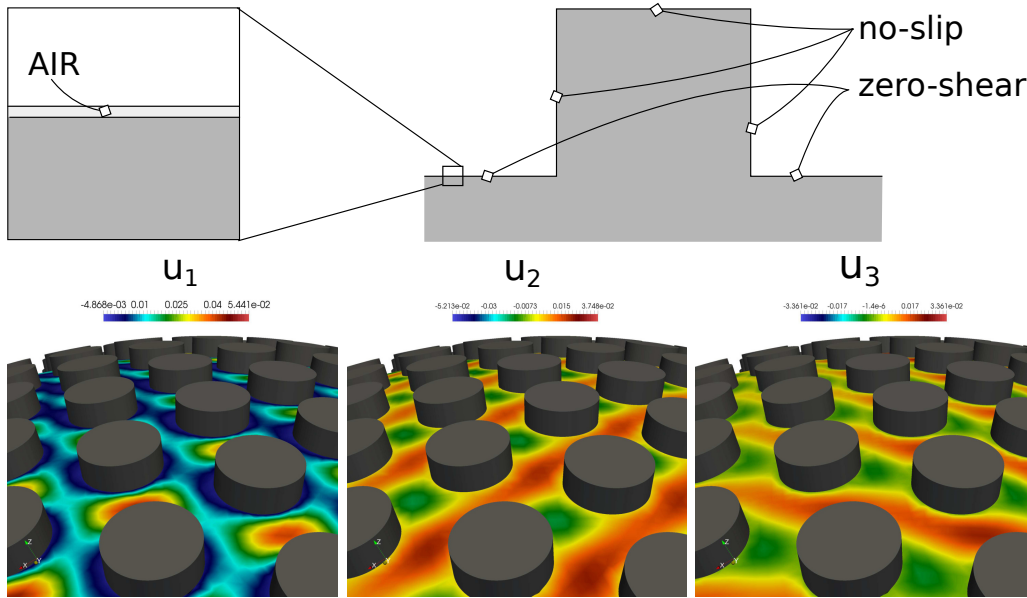


FIGURE 13. The “mixed” configuration used to mimic a partially hydrophobic particle surface. Top: sketch of the configuration with the corresponding boundary conditions. Bottom: fully-resolved fluid flow represented via the iso-contours of the three velocity components in the troughs of the rough layer at a dimensionless radius equal to 1.002.

3.5. Towards drag reduction

The forces acting on the RSP analyzed so far exhibit little variation with respect to those found on the corresponding SSP. It is well known that air entrapped within the cavities of a rough wall can induce a superhydrophobic behaviour of the equivalent surface (Barthlott & Neinhuis 1997; Yang *et al.* 2006). Many strategies aimed at manufacturing such surfaces have recently been developed (cf. Yan *et al.* 2011, for a review). With spheres, a 30% drag reduction obtained thanks to an air plastron entirely covering the surface was reported by Gruncell *et al.* (2013). Polygonal or cylindrical protrusions are a common choice to build surfaces able to trap air, hence to produce a superhydrophobic effect (cf. Philip 1972; Davis & Lauga 2009, 2010; Ng & Wang 2010). This is why it makes sense to examine the potential influence of air entrapment within the rough layer covering a RSP. To keep the problem simple and avoid having to consider a real two-phase flow configuration, we assume that only a nanoscopic air layer stands in the troughs of the cavities, making the corresponding boundary obey a shear-free condition, as sketched in figure 13. This configuration may be seen as a borderline state in which the size of the microscopic air bubbles that filled initially the cavities has decreased drastically due to a long exposure to water (Boinovich *et al.* 2010). Mathematically speaking, in this simplified model the fluid obeys two different boundary conditions at the microscopic level: a succession of no-slip (on the surface of each protrusion) and zero-shear (on the remaining parts of the particle’s surface) conditions is imposed. With this assumption, (2.26) may still be applied, provided that the microscopic problems are suitably modified as described in Appendix A.

Figure 13 displays details of the microscopic velocity field in the region where the no-shear condition is imposed at the particle surface. Thanks to this condition, patches and channels of positive velocities up to 5% of the upstream velocity are seen to subsist in between the protrusions very close to the trough of the cavities. Figure 14 shows that

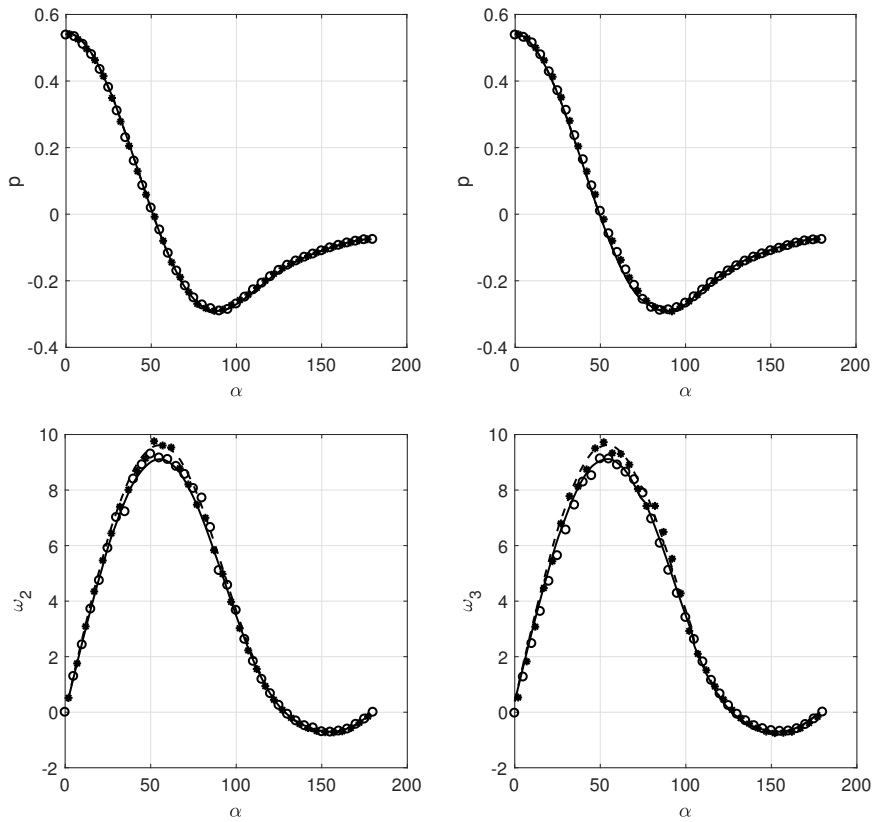


FIGURE 14. Surface pressure and nonzero components of the surface vorticity within the *aa* (left) and *bb* (right) cross-sectional planes. The bullets refer to the results extracted from the DNS with a no-slip condition imposed everywhere on the RSP ($\vartheta = 0.6$ and $\xi = 12$), while the empty circles refer to the “mixed” case. The solid and dashed lines correspond to the quantities computed via the macroscopic model (2.26) with and without the “mixed” microscopic boundary condition.

the “mixed” condition leaves the pressure distribution at the particle surface unchanged, while a small decrease is noticed in the surface vorticity distribution close to the sphere’s equator. This is confirmed by the results of the macroscopic model (solid line in figure 14), based on the modified microscopic tensors calculated as explained in Appendix A. Table 3 summarizes the values of the drag force obtained in each configuration. The “mixed” condition results in a drag reduction less than 2%, essentially due to the slight decrease of the viscous component, F_V . This modest drag reduction is in line with available results obtained by placing axisymmetric baffles at the sphere surface (Grancell *et al.* 2013): in this configuration, only small levels of reduction were observed unless the porosity was increased to 90%, in which case it was noticed that the drag may be reduced by up to 15% for $Re^{out} = 100$.

4. Concluding remarks

The main result of the present paper consists in the macroscopic boundary condition (2.26) applicable to general incompressible flows over microscopically rough surfaces. This condition states that the velocity components tangent to the equivalent smooth wall de-

	F_P	F_V	F_D	
SSP, $R = 1$	0.201	0.228	0.429	
RSP, $\vartheta = 0.6$, $\xi = 12$	0.198	0.228	0.426	
RSP, $\vartheta = 0.6$, $\xi = 12$	mixed	0.197	0.221	0.418
ESP, $R^{eq} = 1$		0.200	0.226	0.426
ESP, $R^{eq} = 1$	mixed	0.199	0.220	0.419

TABLE 3. Drag forces in the case of a SSP and a RSP/ESP, with and without the introduction of “mixed” surfaces (DNS results for the SSP and RSP have been cell-averaged).

pends on two terms, respectively proportional to the tangential pressure gradient and to the strain rate tensor characterizing the outer flow. A second-order surface permeability tensor is associated with the pressure gradient, while a third-order slip tensor is associated with the strain rate. Both tensors depend directly on the local geometry of the rough layer. Within the homogenization-based framework used here, this generalized slip condition appears as the first-order correction to the usual no-slip condition. We assessed its validity via the use of DNS in a non-trivial, fully three-dimensional configuration in the presence of strong inertia effects. The new boundary condition shows better agreement with the DNS results than the classical Navier slip condition, provided that the volume-averaged surface permeability and slip tensors are computed by solving the microscopic problems (2.20) and (2.21). The set of equations governing these problems arise from the development of the boundary condition without further assumptions, thanks to the rational framework provided by the homogenization approach. In particular, the surface permeability \mathcal{K}_{ij} establishes a direct link with the behaviour of a fluid flowing over and through an interface separating a free fluid region from a porous medium (Beavers & Joseph 1967).

While the homogenization approach is most often employed to analyze problems in which time dependency and inertia are both negligible (Barenblatt *et al.* 1960; Allaire 1989), it turns out to be much more flexible in the present case. Indeed, the formal developments presented in §2 and the comparisons carried out for the flow past a rough sphere in §3 demonstrate that the resulting boundary condition works well even in situations characterized by a moderate-to-large Reynolds number. This macroscopic approach is very efficient to save computational effort and time: it greatly simplifies the building of grids aimed at computing flows involving complex surface micro-geometries, and drastically reduces the number of grid cells required to describe the flow structure close to such surfaces. To set ideas, 192 hours on 500 cores at 2.8 Ghz are needed to reach a converged solution of the DNS on the RSP at $Re^{out} = 100$, computed on a grid composed by 2.7×10^7 elements, while for the corresponding macroscopic simulation (ESP) less than 4 hours of computational time are needed with a grid of less than 5 million cells, for a comparable final resolution. When $Re^{out} = 1000$ a statistically converged DNS solution is reached in 720 hours, while the same statistics can be computed on the data provided by the macroscopic simulation in a computational time 20 times smaller. Hence, the wall approximation introduced here is particularly useful if one needs a faster feedback on global quantities such as the drag force. However, it must be pointed out that this condition is only an $\mathcal{O}(\epsilon)$ approximation of the real microscopic condition. In particular, it does not allow the complex behaviour of the flow field at the microscale to be captured, as can easily be concluded by considering the fully-resolved flow within the rough layer

displayed in figures 7 and 13. Two other limitations were encountered in the course of this investigation. First, since the equivalent boundary condition was developed under the assumption $Re^{out} \lesssim \mathcal{O}(\epsilon^{-1})$, it was no surprise to observe that the accuracy of the predictions decreases as larger outer Reynolds numbers, typically of $\mathcal{O}(\epsilon^{-2})$, are considered. More precisely, we found that the equivalent boundary condition is still able to capture correctly the behaviour of the outer flow, but inertia effects cannot be ignored any longer in the calculation of the microscopic tensors if the accuracy has to be maintained close to the surface. Second, the $\mathcal{O}(\epsilon)$ accuracy of the present homogenization approach proved to be insufficient to identify unambiguously the position of the equivalent surface over which (2.26) is to be applied. For instance, in the case of the flow over a sphere considered in §3, the tests carried out with the two limit values of the equivalent radius, R^{inn} and R^{out} , yielded similar results. This indicates that seeking the exact position of the equivalent smooth surface within the interval $[R^{inn}, R^{out}]$ is irrelevant at this level of approximation. A higher-order theory is required if more precision is needed.

With the roughness distribution and the flow regimes considered here, only small variations of the global forces acting on a rough spherical particle were noticed, compared to a smooth sphere of the same size. Nevertheless, the boundary condition (2.26) provides a powerful and versatile tool to optimize the shape and distribution of the protrusions in order to minimize the forces acting over a given overall particle geometry. Another possibility to be explored is that of a modification of the microscopic behaviour of the rough boundary through the introduction of a local hydrophobic treatment. A first step toward that direction was considered in §3.5. The next step could be to consider a thicker air layer filling the entire rough layer, so as to mimic more closely the behaviour of superhydrophobic surfaces. From a modelling point of view, this would require the development of a homogenization approach capable of dealing with two-phase flows (Daly & Roose 2015). Last, as enlightened in §3.1, the lattice employed here to cover the sphere was not strictly homogeneous. More generally, natural surfaces are virtually never perfectly homogeneous. For this reason, one stimulating direction for future research is to deal with the applicability of stochastic extensions of the homogenization theory (Cottetereau 2012; Bella *et al.* 2016) to describe more realistic physical surfaces.

The authors would like to thank the IDEX Foundation of the University of Toulouse for the financial support granted to the last author under the project “Attractivity Chairs”. This work was granted access to the HPC resources of the CALMIP supercomputing center under the allocation 2017-P17021.

Appendix A. Resolution of the microscopic problems and properties of the associated tensors

The surface permeability tensor \mathcal{K}_{ij} and the slip tensor \mathcal{L}_{ijk} are the crucial ingredients for the applicability of (2.26). Physically, they represent the macroscopic counterpart of the microscopic structure: the information about the geometry of the protrusions and their distribution is included there. As already observed, they are defined as the volume average of the tensors obtained by solving problems (2.20) and (2.21), respectively. In this appendix, we show where the values of these tensors, used in the macroscopic simulations, come from, by analyzing them first microscopically and then from an effective point of view. Even though, in principle, (2.20) involves eight equations and eight unknowns ($6 K_{ij}, , 2A_j$), it can be split into two uncoupled Stokes problems with a volume source term, one for (K_{i1}, A_1) and one for (K_{i2}, A_2) . The same can be done with (2.21), where

	\mathcal{K}_{11}	\mathcal{K}_{22}	\mathcal{L}_{113}	\mathcal{L}_{223}
$l_3 = 1$	0.00677	0.00681	0.01134	0.01143
$l_3 = \sqrt{3}$	0.01096	0.0110	0.00975	0.00982
$l_3 = 2\sqrt{3}$	0.02111	0.0212	0.00962	0.00970
$l_3 = 4\sqrt{3}$	0.04064	0.0409	0.00961	0.00970

TABLE 4. Components of the \mathcal{K}_{ij} and \mathcal{L}_{ijk} tensors evaluated with different heights of the microscopic cell ($\vartheta = 0.6$).

the couples (L_{i13}, B_1) and (L_{i23}, B_2) satisfy two Stokes problems with a surface forcing on \mathbb{T} . We refer to Appendix C for details about the numerical resolution of these systems. The sizes of the microscopic cell \mathbb{V} , l_1 , l_2 and l_3 , were introduced in figure 1. When the geometry of the lattice is established, l_1 and l_2 are fixed, while l_3 is still a free parameter with the only constraint that l_3 is of the same order of magnitude as l_1 and l_3 , i.e. we are in the "small roughness" case. However, we have shown in section 3 that the choice of l_3 does not affect the results, provided that they are interpreted correctly. Since neither the theory nor the geometrical construction of the rough surface fixes l_3 , in this section it plays the role of a free parameter on the basis of which the solution is studied. Assuming that each hexagon of the lattice has a side length equal to 1 (normalizing lengths with l) implies that $l_1 = 3$ and $l_2 = \sqrt{3}$, as sketched in figure 1. By construction, the protrusions have a height equal to 1 (which corresponds to the side of the hexagon, i.e. to their radius when $\vartheta = 0$, cf. figure 1).

Figures 15 and 16 are representative of the microscopic behavior of L_{i13} and K_{i1} (B_i and A_i are not shown because they do not play any role in the macroscopic equation at this order in ϵ). The insets in figure 15 display the components of the vector L_{i13} , $i = 1-3$, within \mathbb{V} . Microscopically, the solution exhibits an analogous behaviour for each value of l_3 . A dominant component is found in the direction along which the flow is forced. The other components are antisymmetric with respect to $x_2 = 0$ (L_{213}) or to $x_1 = 0$ (L_{313}). This implies that the corresponding components of the effective tensor are equal to zero. The same conclusion applies to the components K_{3j} of the permeability tensor. These symmetry properties are characteristic of orthotropic geometries, inherited from the cylindrical shape of the protrusions. In the same figure, the variation of \mathcal{L}_{113} with the porosity is described for several prescribed values of l_3 : increasing l_3 , the computed component of the slip tensor reaches an asymptotic value for each ϑ . For a given l_3 , the maximum slip is reached when the porosity is high, i.e. when the cylindrical protrusions become more we have slender. The same happens for \mathcal{L}_{223} , the microscopic distribution of which is not shown since it can be deduced by symmetry.

In figure 16, K_{i1} is seen to exhibit a microscopic behaviour similar to L_{i13} . However its macroscopic behaviour is very different since L_{i13} is observed to depend linearly on l_3 . As shown in §3.1, this is consistent with the theory. Table 4 demonstrates the behaviour of \mathcal{K}_{ij} and \mathcal{L}_{ijk} when l_3 increases, for a porosity set to $\vartheta = 0.6$. The variation of the slip and permeability ratios, $\mathcal{L}_{223}/\mathcal{L}_{113}$ and $\mathcal{K}_{22}/\mathcal{K}_{11}$, with respect to the porosity is displayed in figure 17. It may be seen that the small imperfection in the hexagonal lattice results in a weak anisotropy of the surface coating in the range $0.6 < \vartheta < 1$, especially regarding the permeability tensor. Actually, the ideal transverse isotropy of the cell (diagonal tensors with $\mathcal{L}_{113} = \mathcal{L}_{223}$ and $\mathcal{K}_{11} = \mathcal{K}_{22}$) is reduced to an orthotropic behaviour (diagonal tensors with $\mathcal{L}_{113} \neq \mathcal{L}_{223}$ and $\mathcal{K}_{11} \neq \mathcal{K}_{22}$). The transverse isotropy tends to be restored when $\vartheta \rightarrow 1$.

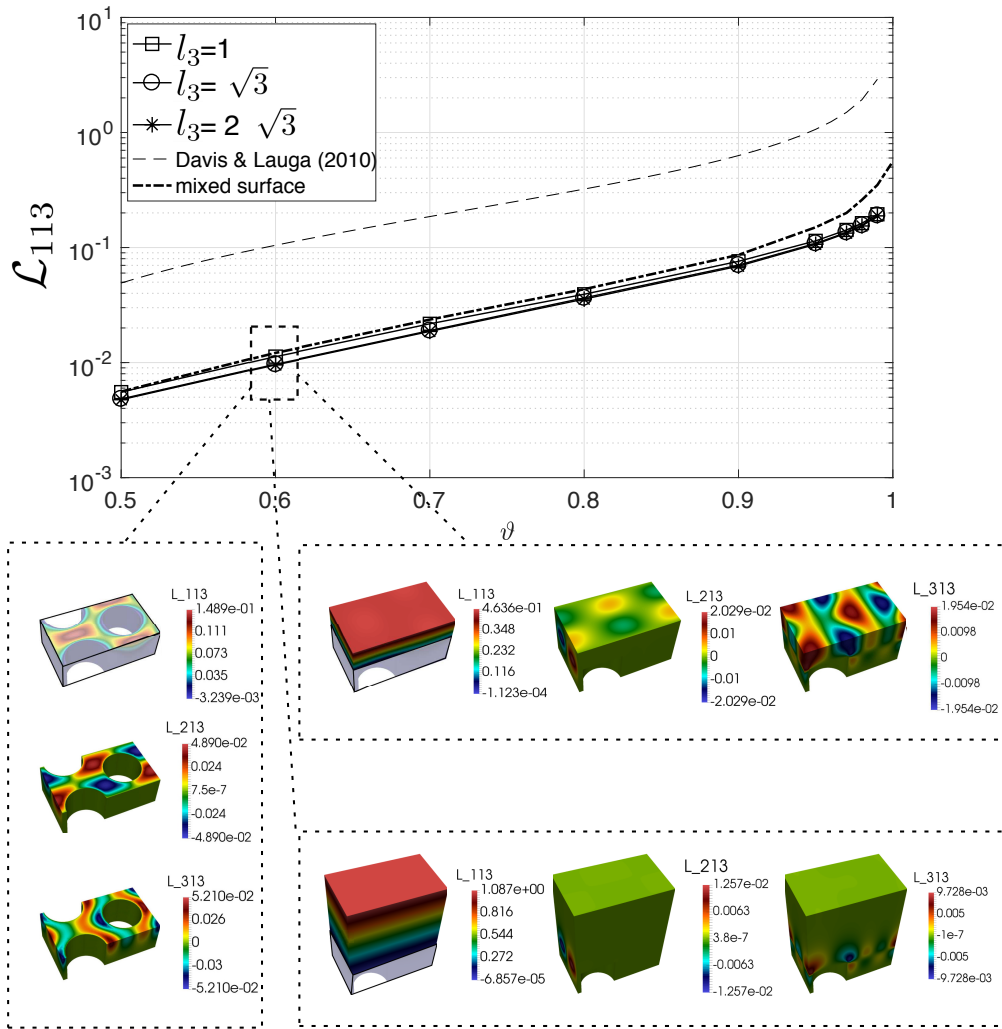


FIGURE 15. Variation of the volume-averaged component \mathcal{L}_{113} with the porosity, ϑ , for different cell heights. As l_3 is increased, the component of the slip tensor becomes constant. The corresponding microscopic components L_{i13} are shown for each l_3 when $\vartheta = 0.6$ (left: $l_3 = 1$, bottom: $l_3 = \sqrt{3}$, top: $l_3 = 2\sqrt{3}$). The antisymmetry of the off-diagonal components, which results in a zero average once (2.23) is applied, is clearly seen in the microscopic solution. Each value in the top frame corresponds to the average over the shadowed region shown in the microscopic visualization of \mathcal{L}_{113} . In the top frame the superhydrophobic results of Davis & Lauga (2010) are shown. Values corresponding to the ‘‘mixed surface’’ are computed using $l_3 = 2\sqrt{3}$.

The validation of the boundary condition (2.26) provided in section 3 also represents a clear validation of the computation of the effective tensors. However, further arguments may be advanced in support to this claim. We compared the slip tensor \mathcal{L}_{ijk} with the results presented by Davis & Lauga (2010), which refer to an ordered distribution of cylinders at a flat, no-shear, gas-liquid interface corresponding to a Cassie-Baxter state. Clearly, this case corresponds to a superhydrophobic behaviour that cannot be realized

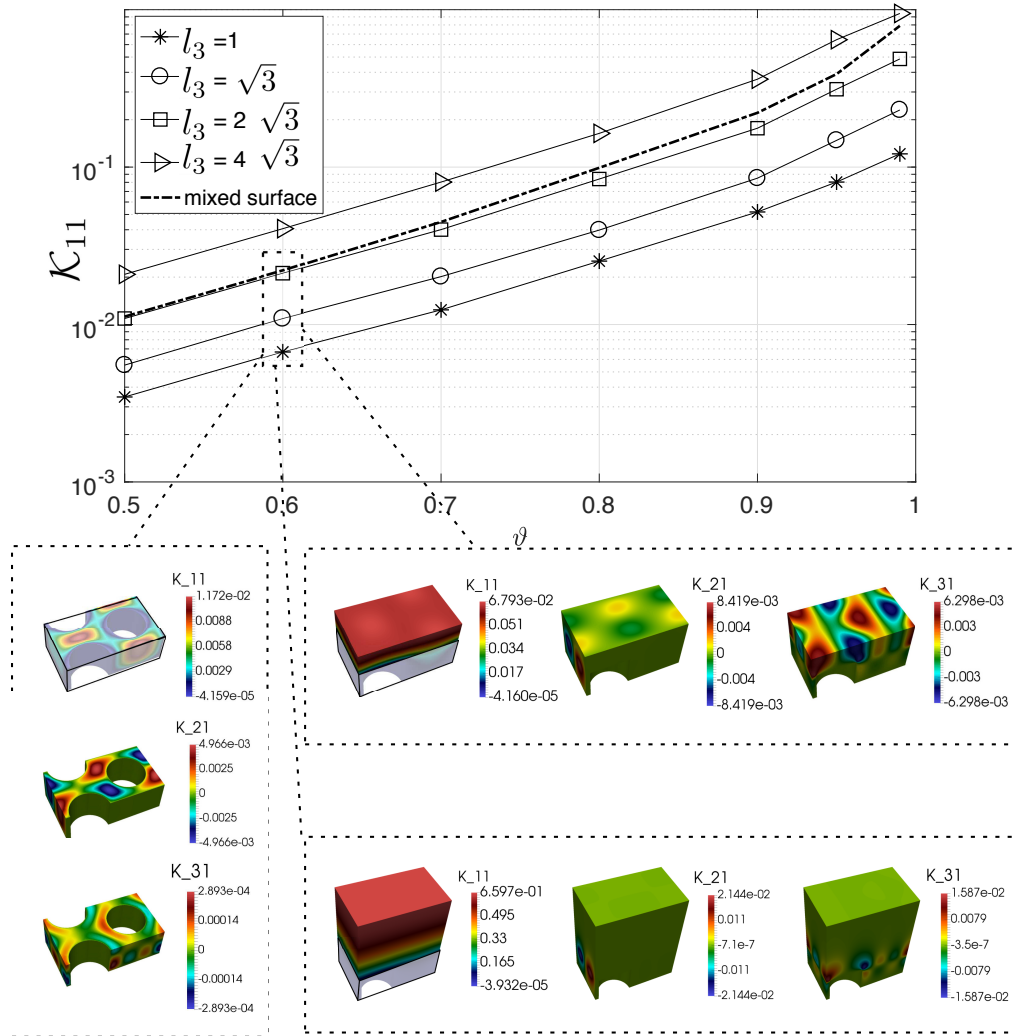


FIGURE 16. Variation of the volume-averaged component K_{11} with the porosity, ϑ , for different cell heights. The components of the surface permeability tensor are proportional to l_3 and no asymptotic behaviour is expected. The corresponding microscopic components K_{i1} are shown for each l_3 when $\vartheta = 0.6$. As for L_{i13} , symmetries cancel out the off-diagonals terms of the averaged tensor. In each case, the average is performed over the shadowed region shown in the microscopic visualization of K_{11} . Values corresponding to the “mixed surface” are computed using $l_3 = 2\sqrt{3}$.

with the Wenzel configuration considered here. This means that the components of the slip tensor found by Davis & Lauga (2010) are necessarily larger than those calculated in the present work. However, figure 15 reveals an important analogy with their results: apart from a multiplicative constant, the function expressing the dependency of \mathcal{L}_{113} with respect to ϑ is the same in both cases. Figure 15 also displays \mathcal{L}_{113} in the case of the “mixed configuration” analyzed in section 3. Here, as already described, the surface of the sphere is hydrophobic (i.e. the fluid satisfies a zero-shear condition), while the surface of the protrusions is hydrophilic (i.e. the fluid satisfies a no-slip condition). As already noticed in section 3, $L_{ijk} = 0$ and $K_{ij} = 0$ are the conditions to be imposed over

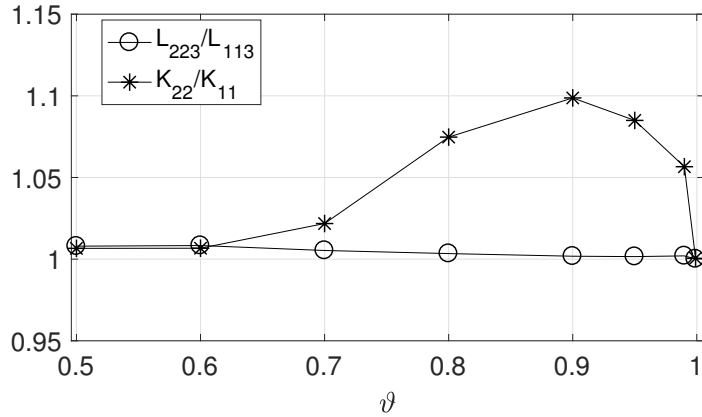


FIGURE 17. Transverse anisotropy induced by the hexagonal lattice: the ratios between the tangential components of the slip tensor (\circ) and the surface permeability tensor (*), all computed with $l_3 = 2\sqrt{3}$, are represented. For each value of ϑ , the components along the second tangential direction ($j = 2$) are slightly larger than those along the first one ($j = 1$). The largest porosity considered is $\vartheta = 0.999$, for which $\mathcal{L}_{223}/\mathcal{L}_{113} = 1.0001$ and $\mathcal{K}_{22}/\mathcal{K}_{11} = 1.0005$.

a hydrophilic wall. In contrast, the shear-free condition over a hydrophobic wall implies that L_{ijk} and K_{ij} have to satisfy the conditions

$$\frac{\partial L_{pl3}}{\partial x_3} + \frac{\partial L_{3l3}}{\partial x_p} = 0 \quad \text{and} \quad \frac{\partial K_{jl}}{\partial x_3} + \frac{\partial K_{3l}}{\partial x_j} = 0, \quad l = 1, 2, \forall j, \quad (\text{A } 1)$$

Solving the microscale problems with the new conditions which represent a combined no-slip/no-shear rough boundary, we recover the values of \mathcal{L}_{113} and \mathcal{K}_{11} denoted as “mixed surface” in figures 15 and 16. Their behaviour with respect to ϑ remains similar to that observed in the hydrophilic case. Particular attention has to be paid to \mathcal{L}_{113} , since the “mixed” case represents a midpoint between the fully hydrophilic case and the situation considered by Davis & Lauga (2010). In our configuration, a second, much less viscous, fluid phase is assumed to cover at a nanoscopic level (not visible at the microscale) the walls over which the zero-shear condition is imposed. In contrast, in Davis & Lauga (2010), a gas completely fills the microscopic rough layer. The nanoscopic layer added here in the “mixed” configuration results in an increase of the components of the slip tensor, which makes our results approach those by Davis & Lauga (2010). As figure 16 shows, the components of the surface permeability tensor \mathcal{K}_{ij} exhibit a qualitatively similar, albeit smaller, increase compared with the Wenzel case (compare the solid-square and dashed-square curves).

Finally, it is of interest to show that this homogenization approach, which provides a rigorous strategy to compute the microscopic tensors, is a flexible tool. Let us say that for some reason, the design of the protrusions has to be modified, assuming that their height remains equal to their radius for each ϑ . This implies that one can consider cells such that $l_3 = l_3(\vartheta)$ is a decreasing function of ϑ . Computing the values of slip and surface permeability tensors in this case yields the curves plotted in figure 18. These curves allow the value of ϑ (close to 0.9 in this case) maximizing \mathcal{L}_{ijk} and \mathcal{K}_{ij} , hence the modulus of the macroscopic slip velocity on the surface, to be readily selected. This is of direct use to design surfaces in view of an optimal drag reduction.

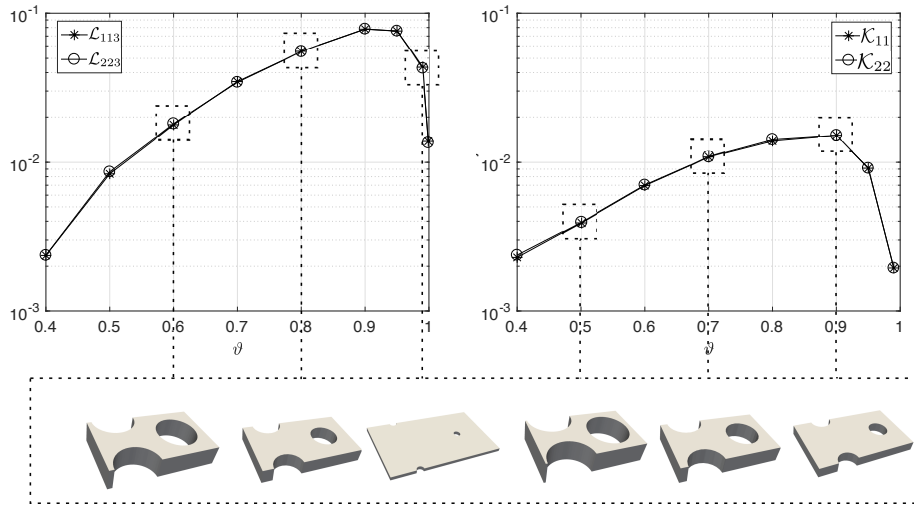


FIGURE 18. Effective slip (left) and surface permeability (right) for protrusions designed in different ways. Sample geometries are represented in the lower frame at different values of the porosity.

Appendix B. Extension of the boundary condition to generic surfaces

Equation (2.26) is a general relation without any limitation on the geometry of the surface to which it is applied. However, the computed surface permeability and slip tensors considered in section 2 referred only to planar surfaces, since we assumed the tangential and normal-to-the-surface directions ($\mathbf{t}_1, \mathbf{t}_2, \mathbf{n}$) vectors to be constant and identical to the Cartesian unit vectors ($\mathbf{e}_1, \mathbf{e}_2, \mathbf{e}_3$). For a non-planar surface \mathbb{S} , (2.20) and (2.21) may still be used provided that

- (a) \mathbb{S} is covered by a periodic lattice;
- (b) the separation of scales is sufficiently large for the curvature of the surface at the microscopic level to be negligible.

Thanks to (a), \mathcal{K}_{ij} and \mathcal{L}_{ijk} are constant if expressed in terms of the local frame built on the tangent and normal unit vectors ($\mathbf{t}_1, \mathbf{t}_2, \mathbf{n}$), but this is no longer the case if the coordinate system is changed to an arbitrary one. Thanks to (b), problems (2.20) and (2.21) yield

$$\mathcal{K} = \mathcal{K}_{11} \mathbf{t}_1 \wedge \mathbf{t}_1 + \mathcal{K}_{22} \mathbf{t}_2 \wedge \mathbf{t}_2 \quad (\text{B } 1)$$

and

$$\mathcal{L} = \mathcal{L}_{113} \mathbf{t}_1 \wedge \mathbf{t}_1 \wedge \mathbf{n} + \mathcal{L}_{223} \mathbf{t}_2 \wedge \mathbf{t}_2 \wedge \mathbf{n}, \quad (\text{B } 2)$$

where \wedge denotes the tensor product ($\mathbf{a} \wedge \mathbf{b} := a_i b_j$). To express \mathcal{K}_{ij} and \mathcal{L}_{ijk} in Cartesian coordinates, as in (2.26), we need the mapping

$$\Xi : \mathbb{R}^3 \rightarrow \mathbb{S} \quad \text{such that} \quad (\mathbf{e}_1, \mathbf{e}_2, \mathbf{e}_3) \rightarrow (\mathbf{t}_1, \mathbf{t}_2, \mathbf{n}). \quad (\text{B } 3)$$

Applying Ξ to (B 1) and (B 2), we find the Cartesian expression of the tensor components. In particular, by virtue of the \wedge definition, the symmetry properties remain unaltered. In the present case, these symmetries read

$$\mathcal{K}_{ij} = \mathcal{K}_{ji} \quad \text{and} \quad \mathcal{L}_{ijk} = \mathcal{L}_{jik} = \mathcal{L}_{ikj}. \quad (\text{B } 4)$$

n	\mathcal{L}_{113}	\mathcal{K}_{11}
25	0.00933	0.01908
50	0.00962	0.02112
100	0.00962	0.02111

TABLE 5. Spatial convergence of \mathcal{L}_{113} and \mathcal{K}_{11} with respect to the grids shown in figure 19 and $l_3 = 2\sqrt{3}$. The number n refers to the number of cells per unit length.

In section 3 we used (2.26) to impose a nonzero slip over a sphere. In this case, the transformation Ξ is

$$\hat{\theta} = \mathbf{t}_1(\mathbf{e}_1, \mathbf{e}_2, \mathbf{e}_3) = -\sin \theta \mathbf{e}_1 + \cos \phi \mathbf{e}_2, \quad (\text{B } 5)$$

$$\hat{\phi} = \mathbf{t}_2(\mathbf{e}_1, \mathbf{e}_2, \mathbf{e}_3) = \cos \theta \cos \phi \mathbf{e}_1 + \sin \theta \cos \phi \mathbf{e}_2 - \sin \phi \mathbf{e}_3, \quad (\text{B } 6)$$

$$\hat{r} = \mathbf{n}(\mathbf{e}_1, \mathbf{e}_2, \mathbf{e}_3) = \cos \theta \cos \phi \mathbf{e}_1 + \sin \theta \cos \phi \mathbf{e}_2 - \sin \theta \mathbf{e}_3, \quad (\text{B } 7)$$

where the angles θ and ϕ identify the position on the sphere surface and write in Cartesian coordinates $\theta = \tan^{-1}(x_2/x_1)$ for $x_2 \geq 0$ or $\theta = -\tan^{-1}(x_2/x_1)$ for $x_2 < 0$ and $\phi = \cos^{-1}(x_3/R)$. Substituting (B 5), (B 6) and (B 7) in (B 1) and (B 2), we obtain \mathcal{K} and \mathcal{L} for a spherical surface.

In section 2 we noticed that the wall normal velocity is zero in (2.25) if the no-slip condition applies. This behaviour is valid also after a change of coordinates. This is easily verified by noting that $\mathbf{t}_1 \cdot \mathbf{n} = \mathbf{t}_2 \cdot \mathbf{n} = 0$ and, consequently,

$$\mathbf{n} \cdot \mathbf{t}_1 \wedge \mathbf{t}_1 \wedge \mathbf{n} = \mathbf{n} \cdot \mathbf{t}_2 \wedge \mathbf{t}_2 \wedge \mathbf{n} = 0. \quad (\text{B } 8)$$

Projecting (2.26) along \mathbf{n} and using (B 8), the normal velocity component is seen to vanish.

Appendix C. Technical aspects of the computations

The numerical solutions discussed in this paper were obtained using the finite volume open software OpenFOAM (<http://www.openfoam.org>). In this appendix we summarize the issues related to the numerical solution of the microscopic and macroscopic problems.

C.1. Implementation of the condition (2.26)

To compute the flow past the ESP, the boundary condition (2.26) was transformed into a non-homogeneous Neumann condition by implementing it in the explicit iterative form

$$\frac{\partial u_i^{(m)}}{\partial x_j} n_j = \frac{\partial u_i^{(m-1)}}{\partial x_j} n_j - u_i^{(m-1)} - \epsilon^2 Re^{out} \mathcal{K}_{ij} \frac{\partial p^{(m-1)}}{\partial x_j} + \epsilon \mathcal{L}_{ilk} \left(\frac{\partial u_l^{(m-1)}}{\partial x_k} + \frac{\partial u_k^{(m-1)}}{\partial x_l} \right) |_{\text{ES}}, \quad (\text{C } 1)$$

where m denotes the temporal index and n_j is the outer normal to the ES surface.

C.2. Convergence of the microscopic results

The spatial convergence of the steady solution of problems (2.20) and (2.21) was checked. Figure 19 displays three different spatial discretizations of the microscopic cell for the case $\vartheta = 0.6$. The grids were built with the routine *snappyHexMesh* using $n = 25, 50$ and 100 cells per unit length, respectively. The values of \mathcal{L}_{113} and \mathcal{K}_{11} reported in table 5 are computed with a cell such that $l_3 = 2\sqrt{3}$ and indicate convergence for $n = 50$.

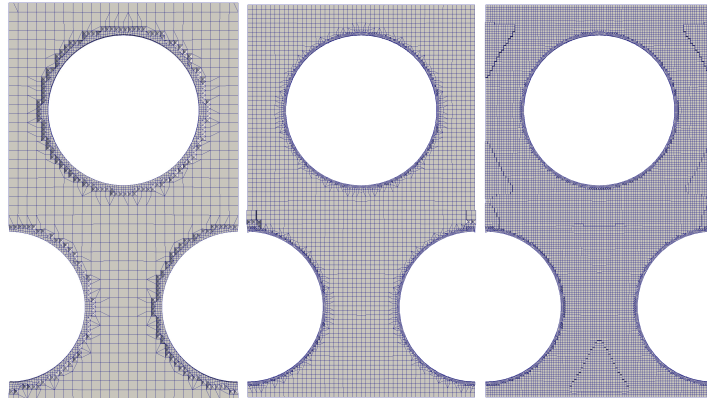


FIGURE 19. Cut of the microscopic elementary cell at $x_3 = 0.5$. The three different grids used to test the spatial convergence are displayed. They involve 25, 50 and 100 cells per unit length, respectively.

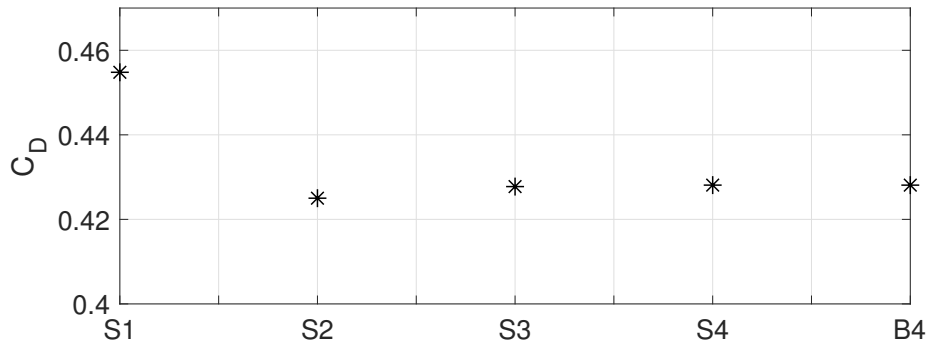


FIGURE 20. Drag force on a SSP in the case of “small” (S) and “big” (B) computational domains ($Re^{out} = 100$). The numbers on the x -axis denote different grid resolutions: from 1.8×10^4 cells (1) to 6.2×10^6 cells (4).

C.3. Validation of the macroscopic configuration and convergence of the results

To validate the solver used to compute the flow past both RSP and ESP, we considered the flow past a SSP, with a no-slip condition at its surface and $Re^{out} = 100$. Figure 20 shows the total drag force (F_D) acting on a sphere with unit radius, when the resolution and the size of the computational domain are varied. The configurations denoted with “S” refer to a small domain with size $100 \times 40 \times 40$, while “B” stands for a bigger domain with size $200 \times 80 \times 80$. The numbers refer to different grid resolutions. After having confirmed grid convergence for the S configuration, we checked the influence of the domain size by switching to the B configuration. As can be inferred from the figure, the S3 configuration already estimates the drag force acting on the SSP well.

C.4. Evaluation of the forces on the RSP

The DNS of the flow past a RSP was also carried out using OpenFOAM. Two computational domains were employed, made respectively of approximately 1.5×10^7 and 2.7×10^7 cells. No significant change in the local and global forces acting on the particle

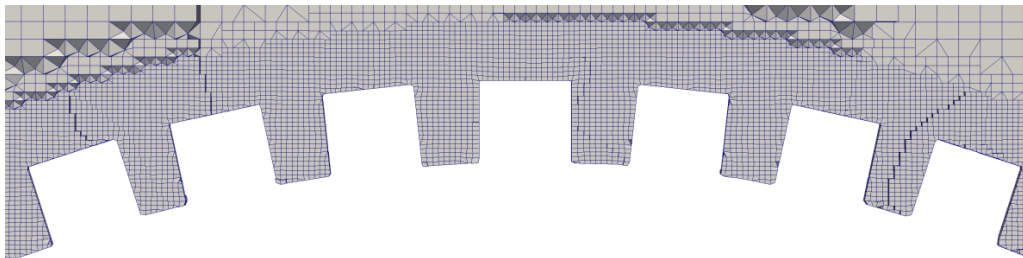


FIGURE 21. Zoom of the computational grid around a RSP, composed of 2.7×10^7 cells.

was noticed. The large number of computational cells is required to properly solve the fluid flow at the scale of the protrusions. A zoom of the grid close to the particle surface is provided in figure 21. In this case, the grid is made of 2.7×10^7 cells and the code is run using 500 cores in parallel.

To determine the forces at the particle surface, two methods were used. The first of them is characteristic of a pointwise approach, with pressure and viscous forces evaluated over each cell of the computational grid used to discretize the surface, then integrated over the whole RSP. The corresponding values (shown in table 1) are meaningful only in a pointwise sense. Considering these forces over a complex surface with microscopic asperities in a macroscopic environment would not make sense.

The second method is the macroscopic counterpart of the above approach. It consists of the following steps:

- the rough layer is divided into elementary microscopic cells;
- pressure and viscous stresses are integrated over each cell;
- since the ensemble of the microscopic cells cover the whole surface of the spherical particle, each cell is univocally identified with a portion of the smooth sphere underlying the rough layer (which ideally corresponds to a macroscopic point); this allows an accurate mapping between the RSP and the ESP to be established;
- the averaged forces are projected onto the portions of the ESP identified at the previous step;
- the values obtained through this projection are integrated over the ESP surface.

This procedure, the results of which are shown in table 2, makes it possible to compute “macroscopic” forces acting on a RSP comparable with those obtained by imposing (2.26) on the surface of the ESP.

REFERENCES

- ALLAIRE, G. 1989 Homogenization of Stokes flow in a connected porous medium. *Asymp. Anal.* **2**, 203–222.
- AMIRAT, Y., BRESCH, D., LEMOINE, J. & SIMON, J. 2001 Effect of rugosity on a flow governed by stationary Navier-Stokes equations. *Quart. J. Appl. Math.*, **59**, 769–785.
- BARENBLATT, G.I., ZHELTOV, I.P. & KOCHINA, I.N. 1960 Basic concepts in the theory of seepage of homogeneous liquids in fissured rocks. *J. Appl. Math. Mech.* **24**, 1286–1303.
- BARTHLOTT, W. & NEINHUIS, C. 1997 Purity of the sacred lotus, or escape from contamination in biological surfaces. *Planta* **202**, 1–8.
- BAZANT, M. Z. & VINOGRADOVA, O. I. 2008 Tensorial hydrodynamic slip. *J. Fluid Mech.* **613**, 125–134.
- BELLA, P., FERHMAN, B., FISCHER, J. & OTTO, F. 2016 Stochastic homogenization of linear elliptic equations: Higher-order error estimates in weak norms via second-order correctors. *arXiv:1609.01528*.

- BEAVERS, G. S. & JOSEPH, D. D. 1967 Boundary condition at a natural permeable wall. *J. Fluid Mech.* **30**, 197–207.
- BECHERT, D. W. & BARTENWERFER, M. 1989, The viscous flow on surfaces with longitudinal ribs. *J. Fluid Mech.* **206**, 105–129.
- BHIRDE, A. A., PATEL, V., GAVARD, J., ZHANG, G., SOUSA, A. A., MASEDUNSKAS, R., LEAPMAN, D., WEIGERT, R., GUTKIND, J. S. & RUSLING, J. F. 2009 Targeted killing of cancer cells in vivo and in vitro with EGF-directed nanotube-based drug delivery. *ACS Nano* **3**, 307–316.
- BHUSHAN, B. & JUNG, Y. C. 2011 Natural and biomimetic artificial surfaces for superhydrophobicity, self-cleaning, low adhesion, and drug reduction. *Prog. Mater. Sci.* **56**, 1–108.
- BOCQUET, L. & BARRAT, J. L. 2007 Flow boundary conditions from nano- to micro-scales. *Soft Matter* **3**, 685–693.
- BOCQUET, L. & LAUGA, E. 2011 A smooth future?. *Nature Mater.* **10**, 334337.
- BOINOVICH, L., EMELYANENKO, A. M. & PASHININ, A. S. 2010 Analysis of long-term durability of superhydrophobic properties under continuous contact with water. *ACS Appl. Mater. Interfaces* **2**, 1754–1758.
- COTTEREAU, R. 2013 A stochastic-deterministic coupling method for multiscale problems. Application to numerical homogenization of random materials. *Procedia IUTAM* **6**, 35–43.
- COTTIN-BIZONNE, C., BARENTIN, C. & BOCQUET, L. 2012 Scaling laws for slippage on superhydrophobic fractal surfaces. *Phys. Fluids* **24**, 012001.
- DALY, K.R. & ROOSE, T. 2015 Homogenization of two fluid flow in porous media. *Proc. Roy. Soc. A* **471**, 20140564.
- DAVIS, A. M. J. & LAUGA, E. 2010 The friction of a mesh-like super-hydrophobic surface. *Phys. Fluids* **21**, 113101.
- DAVIS, A. M. J. & LAUGA, E. 2010 Hydrodynamic friction of fakir-like superhydrophobic surfaces. *J. Fluid. Mech.* **661**, 402–411.
- DE NICOLA, F., CASTRUCCI, P., SCARSELLI, M., NANNI, F., CACCIOTTI, I. & DE CRESCENZI, M. 2015 Multi-fractal hierarchy of single-walled carbon nanotube hydrophobic coatings. *Sci. Rep.* **5**, 8583.
- GOH, P. S., ISMAIL, A. F. & NG, B. C. Carbon nanotubes for desalination: Performance evaluation and current hurdles. *Desalination* **308**, 2–14.
- GRUNCELL, B. R. K., SANDHAM, N. D. & MCRAE, G. Simulations of laminar flow past a superhydrophobic sphere with drag reduction and separation delay. *Phys. Fluids* **25**, 043601.
- GUO, J., VERAN-TISSOIRES, S. & QUINTARD, M. 2016 Effective surface and boundary conditions for heterogeneous surfaces with mixed boundary conditions. *J. Comput. Phys.* **305**, 942–963.
- INTROINI, C., QUINTARD, M. & DUVAL, F. 2011 Effective surface modeling for momentum and heat transfer over rough surfaces: application to a natural convection problem. *Int. J. Heat Mass Transf.* **54**, 3622–3641.
- JIMÉNEZ BOLAÑOS, S. & VERNESCU, B. 2017 Derivation of the Navier slip and slip length for viscous flows over a rough boundary. *Phys. Fluids* **29**, 057103.
- KAMRIN, K., BAZANT, M. & STONE, H.A. 2010 Effective slip boundary conditions for arbitrary periodic surfaces: the surface mobility tensor. *J. Fluid Mech.* **658**, 409–437.
- LĀCIS, U. & BAGHERI, S. 2017 A framework for computing effective boundary conditions at the interface between free fluid and a porous medium. *J. Fluid Mech.* **812**, 866–889.
- LĀCIS, U., ZAMPOGNA, G. A. & BAGHERI, S. 2017 A computational continuum model of poroelastic beds. *Proc. Roy. Soc. A-Math. Phys. Eng. Sci.* **473**, 20160932.
- LAUGA, E., BRENNER, M. P. & STONE, H. A. 2005 Microfluidics: The no-slip boundary condition. In *Handbook of Experimental Fluid Dynamics* (ed. J. Foss, C. Tropea & A. Yarin), chap. 15. Springer.
- LAUGA, E. & STONE, H. A. 2003 Effective slip in pressure-driven Stokes flow. *J. Fluid Mech.* **489**, 55–77.
- LEE, C. K. & MEI, C. C. Thermal consolidation in porous media by homogenization theory – Derivation of macroscale equation. *Adv. Water Res.* **20**, 127–144.
- LIAKOPOULOS, A., SOFOS, F. & KARAKASIDIS, T. E. 2017 Darcy-Weisbach friction factor at the nanoscale: From atomistic calculations to continuum models. *Phys. Fluids* **29**, 052003.

- LUCHINI, P., MANZO D. & POZZI, A. 1991 Resistance of a grooved surface to parallel flow and cross-flow. *J. Fluid Mech.* **228**, 87–109.
- LUCHINI, P. 2013 Linearized no-slip boundary conditions at a rough surface. *J. Fluid Mech.* **737**, 349–367.
- MAJUMDER, M., CHOPRA N., ANDREWS R. & HINDS, B. J. 2005 Nanoscale hydrodynamics: enhanced flow in carbon nanotubes. *Nature* **438**, 44–44.
- MARTINI, A., ROXIN A., SNURR R. Q., WANG Q. & LICHTER, S. 2008 Molecular mechanisms of liquid slip. *J. Fluid Mech.* **600**, 257–269.
- MEI, C. C. & VERNESCU, B. 2010 *Homogenization Methods for Multiscale Mechanics*. World Scientific, Singapore.
- NAVIER, C. L. M. H. 1823 Mémoires sur les lois du mouvement des fluides. *Mém. Acad. Sci. Inst. France*, **6**, 389–416.
- NG, C.O. & WANG, C.Y. 2010 Apparent slip arising from Stokes shear flow over a bidimensional patterned surface. *Microfluid. Nanofluid.* **8**, 361–371.
- ONDA, T., SHIBUCHI, S., SATOH, N. & TSUJII, K. 1996 Super-water-repellent fractal surfaces. *Langmuir* **12**, 2125–2127.
- ORR, T. S., DOMARADZKI, J. A., SPEDDING, G. R. & CONSTANTINESCU, G. S. 2015 Numerical simulations of the near wake of a sphere moving in a steady, horizontal motion through a linearly stratified fluid at $Re = 1000$. *Phys. Fluids* **27**, 035113.
- PASQUIER, S., QUINTARD, M. & DAVIT, Y. 2017 Modeling flow in porous media with rough surfaces: effective slip boundary conditions and application to structured packings. *Chem. Eng. Sci.* **165**, 131–146.
- PHILIP, J.R. 1972 Flows satisfying mixed no-slip and no-shear conditions. *J. Appl. Math. Phys. (ZAMP)* **23**, 353–372.
- REHMAN, N. M. A., KUMAR, A. & SHUKLA, R. K. 2017 Influence of hydrodynamic slip on convective transport in flow past a circular cylinder. *Theor. Comput. Fluid Dyn.*, **31**, 251–280.
- ROTHSTEIN, J. P. 2010 Slip on superhydrophobic surfaces. *Annu. Rev. Fluid Mech.*, **42**, 89–109.
- SARKAR, K. & PROSPERETTI, A. 1996 Effective boundary conditions for Stokes flow over a rough surface. *J. Fluid Mech.* **316**, 223–240.
- WALSH M. J. 1983 Riblets as a viscous drag reduction technique. *AIAA J.* **21**, 485–485.
- VERAN, S., ASPA, Y. & QUINTARD, M. 2009 Effective boundary conditions for rough reactive walls in laminar boundary layers. *Int. J. Heat Mass Transf.* **52**, 3712–3725.
- VERSTEEG, H. K. & MALALASEKERA, W. 2007 An introduction to Computational Fluid Dynamics. The Finite Volume Method. Pearson Education Limited, Harlow, Essex UK.
- YAN, Y.Y., GAO, N. & BARTHLOTT, W. 2011 Mimicking natural superhydrophobic surfaces and grasping the wetting process: A review on recent progress in preparing superhydrophobic surfaces. *Adv. Colloid Interface Sci.* **162**, 80–105.
- YANG, C., TARTAGLINO, U & PERSSON, B.N.J 2006 Influence of surface roughness on superhydrophobicity. *Phys. Rev. Lett.* **97**, 116103.
- YBERT, C. & BARENTIN, C. & COTTIN-BIZONNE, C. 2007 Achieving large slip with superhydrophobic surfaces: Scaling laws for generic geometries. *Phys. Fluids* **19**, 123601.
- ZAMPOGNA, G. A. & BOTTARO, A. 2016 Fluid flow over and through a regular bundle of rigid fibres. *J. Fluid. Mech.* **792**, 1–31.